Neural circuit pathology driven by *Shank3* mutation disrupts social behaviors

Sunwhi Kim[1,2],

Yong-Eun Kim[1,2],

Inuk Song[3],

Yusuke Ujihara[1,2],

Namsoo Kim[4],

Yong-Hui Jiang[5],

Henry H. Yin[6],

Tae-Ho Lee[3],

Il Hwan Kim[1,2,7,*]

[1]Department of Anatomy and Neurobiology, University of Tennessee Health Science Center, Memphis, TN 38163, USA

[2]Neuroscience Institute, University of Tennessee Health Science Center, Memphis, TN 38163, USA

[3]Department of Psychology, Virginia Tech, Blacksburg, VA 24061, USA

[4]Janelia Research Campus, Howard Hughes Medical Institute, Ashburn, VA 20147, USA

[5]Department of Genetics, Pediatrics and Neuroscience, Yale University School of Medicine, New Haven, CT 06520, USA

[6]Department of Psychology and Neuroscience, Duke University, Durham, NC 27708, USA

[7]Lead contact

SUMMARY

Dysfunctional sociability is a core symptom in autism spectrum disorder (ASD) that may arise from neural-network dysconnectivity between multiple brain regions. However, pathogenic neural-

network mechanisms underlying social dysfunction are largely unknown. Here, we demonstrate that circuit-selective mutation (ctMUT) of ASD-risk *Shank3* gene within a unidirectional projection from the prefrontal cortex to the basolateral amygdala alters spine morphology and excitatory-inhibitory balance of the circuit. Shank3 ctMUT mice show reduced sociability as well as elevated neural activity and its amplitude variability, which is consistent with the neuroimaging results from human ASD patients. Moreover, the circuit hyper-activity disrupts the temporal correlation of socially tuned neurons to the events of social interactions. Finally, optogenetic circuit activation in wild-type mice partially recapitulates the reduced sociability of *Shank3* ctMUT mice, while circuit inhibition in *Shank3* ctMUT mice partially rescues social behavior. Collectively, these results highlight a circuit-level pathogenic mechanism of *Shank3* mutation that drives social dysfunction.

Graphical Abstract
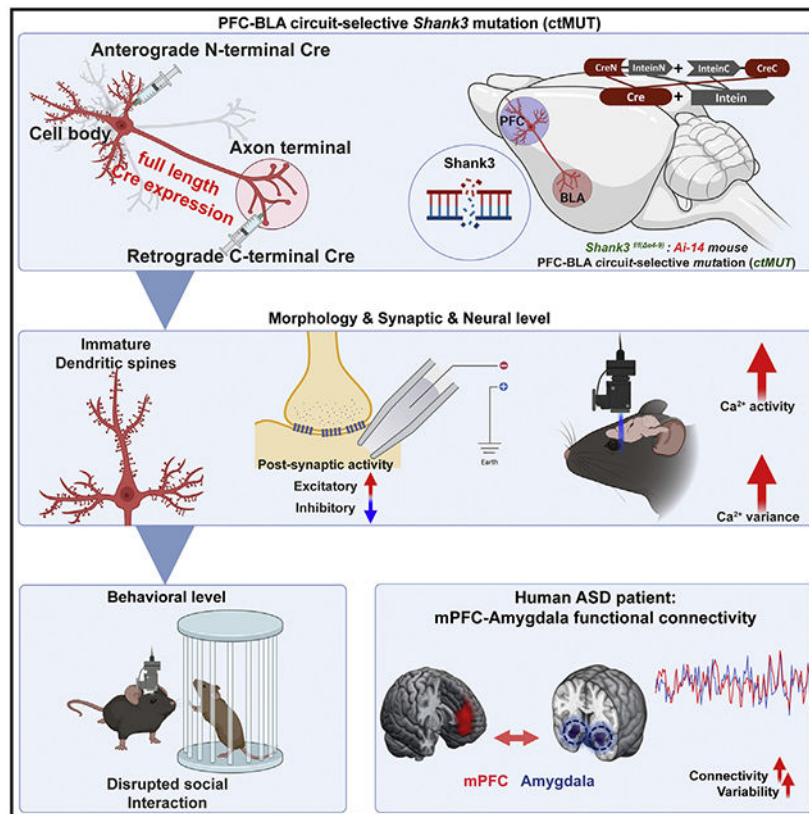
In brief

Kim et al. report that deletion of *Shank3*, an autism risk gene exclusively within the PFC-BLA circuit, results in social dysfunction and disrupts social-behavior-tuned circuit activity by hyper-activation. Similar PFC-BLA hyper-connectivity is also observable in human ASD patients.

INTRODUCTION

Disability in social interaction is one of the most common yet devastating symptoms observed in many neurological disorders including schizophrenia, depression, and autism spectrum disorder (ASD) that is often associated with risk-gene mutations (Kennedy and Adolphs, 2012). Unfortunately, there are limited treatments for impaired social behaviors due to a lack of understanding of how risk genes alter the neural system to affect social behavior. Previous studies in human and non-human primates suggest that social behaviors are mediated by a large and distributed neural network with multiple brain regions (Kennedy and Adolphs, 2012; Sliwa and Freiwald, 2017). Despite the availability of animal models that manipulate risk genes at the level of the whole brain, specific brain regions (Guo et al., 2019; Bey et al., 2018), or specific cell types (Tsien et al., 1996), little is known about how these genes affect specific neural circuits involved in social behavior. To address this gap in our knowledge, a neural-circuit-level strategy is required to decipher the network mechanisms underlying the risk-gene-driven social deficits. Thus, in the present study, we exploit an interregional neural-connectivity approach by manipulating an ASD risk gene in a specific neural circuit *in vivo*.

SH3 and multiple ankyrin repeat domains 3 (SHANK3), also known as proline-rich synapse-associated protein 2 (ProSAP2), is a major scaffolding protein enriched in the post-synaptic density of excitatory neurons (Jiang and Ehlers, 2013). *Shank3* has been investigated as a risk gene for Phelan-McDermid syndrome, schizophrenia, intellectual disability, and ASD (Monteiro and Feng, 2017). *Shank3* deficiency represents a monogenic ASD risk factor involved in about 1% of individuals with ASD (Moessner et al., 2007; Leblond et al., 2014; Durand et al., 2007). Various *Shank3* mutant animal models display cellular and behavioral deficiencies relevant to symptoms of human ASD patients, including altered neuronal morphology, disrupted neuronal physiology, and abnormal behaviors including social interaction, repetitive behaviors, and cognitive- and motor-performance disturbances (Peça et al., 2011; Jaramillo et al., 2016; Wang et al., 2016; Bozdagi et al., 2010; Zhou et al., 2019; Monteiro and Feng, 2017; Yoo et al., 2019; Yi et al., 2016; Lee et al., 2015). For instance, *Shank3* mutant mouse models of disrupting major SHANK3 isoforms (SHANK3α and β) display aberrant social behaviors, motor coordination, and increased repetitive behaviors (Wang et al., 2011).

The prefrontal cortex (PFC) has been implicated in social behaviors both in humans (Bicks et al., 2015; Adolphs, 2003; Forbes and Grafman, 2010; Grossmann, 2013; Amodio and Frith, 2006) and animal models (Liang et al., 2018; Bicks et al., 2015; Lee et al., 2016). Studies with human patients and animal models of ASD have shown abnormal excitability and connectivity of the PFC (Nelson and Valakh, 2015; Gilbert et al., 2008; Huang et al., 2016; Pagani et al., 2019). The PFC projects to multiple brain regions including nucleus accumbens, hippocampus, brainstem, substantia nigra, and amygdala (Bossert et al., 2012; Barker et al., 2017; Franklin et al., 2017; Kim et al., 2015a; Hultman et al., 2016; Murugan et al., 2017). Notably, optogenetic activation of the circuit between the PFC and amygdala of wild-type (WT) mice decreased social interaction (Huang et al., 2020; Felix-Ortiz et al., 2016). Moreover, we have recently reported that the disruption of Arp2/3 complex, a key cytoskeletal regulator in the PFC circuit projecting to the basolateral part of the amygdala

(BLA), alters the morphology of dendritic spines and increases neural activity, leading to decreased social preference (Kim et al., 2013, 2015a, 2020). These findings demonstrate the importance of the PFC-BLA circuit in social behaviors.

In the present study, using an advanced circuit-selective gene-manipulating tool and conditional *Shank3* [e4-9] mice (Wang et al., 2011), we specifically deleted the major isoforms of SHANK3 in the PFC-BLA circuit. Using this *Shank3* [e4-9] circuit-selective mutant (ctMUT) mouse model, we found that the ctMUT mice display altered neuronal morphology, increased post-synaptic excitatory activity, and reduced inhibitory activity. Moreover, *in vivo* endoscopic Ca^{2+} imaging revealed reduced sociability as well as elevated neural activity and variability in the PFC-BLA circuit of ctMUT mice. Importantly, human neuroimaging data from ASD individuals also showed similar results. Analysis of neural signals in mice revealed the existence of socially tuned neurons in the PFC-BLA circuit and that their temporal correlations to social behaviors were reduced by *Shank3* [e4-9] ctMUT. Finally, optogenetic-activation-induced hyperactivity of the PFC-BLA circuit in WT mice partially emulated some of the abnormal social behaviors seen in the ctMUT mice; meanwhile, circuit inhibition of the ctMUT mice partially rescued social behaviors. Collectively, this study reveals a pathogenic neural-circuit mechanism underlying social behavioral deficits driven by the ASD risk factor *Shank3* mutation.

RESULTS

Shank3 mutation in the PFC-BLA neural circuit

To precisely observe a gene mutation effect on a neural circuit, a methodology enabling a selective gene mutation within a specific circuit is needed. Thus, we developed an advanced circuit-specific Cre-expressing system by innovating our previous strategy (Kim et al., 2020). Using a combination of split-Intein-mediated split-Cre reconstitution mechanism (Wang et al., 2012) and adeno-associated virus (AAV)-mediated bidirectional gene transduction system including anterograde AAV8 encoding an N-terminal Cre fused with an N-terminal Intein (AAV8-*CreN-InteinN*; from cell-body region) and retrograde AAV (Tervo et al., 2016) encoding a C-terminal Intein fused with a C-terminal Cre (AAV retro-*InteinC-CreC*; from axonal terminal region) (Figure 1A), we achieved robust, highly specific, and circuit-selective expression of Cre in a unidirectional neural circuit. The specificity of this Intein-mediated Cre-expressing system was validated by HEK293T cells *in vitro* (Figures S1A-S1C). To delete major isoforms of SHANK3 in the PFC-BLA circuit and visualize the mutant circuit, we expressed Cre in the PFC-BLA circuit by injecting AAV8-*CreN-InteinN* in the PFC and AAV retro-*InteinC-CreC* in the BLA of *Shank3*[f/f (e4-9)] (hereafter *Shank3*[f/f]): *Ai-14* (Cre reporter) double-mutant mice (Figure 1B). Two weeks after the injections, Cre-reporting tdTomato signals were found in the cell bodies of PFC (Figure 1D) and axonal fibers in the striatum and BLA (Figures 1E-1G), confirming exclusive expression of Cre within the unidirectional circuit from PFC to BLA. We also confirmed that CreN itself has no enzymatic activity (Figures S2A-S2C). Next, we compared our circuit-selective split-Cre system with conventional region-specific Cre expression (AAV-*Cre*). We injected AAV9-*Cre* into the PFC of *Ai-14* mice and found tdTomato-positive axonal fibers in various regions throughout the brain (Figures S2D-S2F),

reflecting the circuit selectivity of our strategy. The split-Cre reconstitution system also showed higher specificity and sensitivity compared with conventional retrograde tracer cholera toxin subunit B (CTB) injected into the BLA (Figures S2J-S2R).

We also tested an AAV9 serotype (instead of AAV8) for expressing CreN-InteinN in the PFC with AAV retro-*InteinC-CreC* injection in the BLA. This combination expressed the Cre in cell bodies not only in the PFC but also in the BLA (Figures S2G-S2I), presumably due to the spontaneous transsynaptic translocation (Zingg et al., 2017), suggesting that both PFC-BLA circuit neurons and a subset of recipient neurons in BLA express Cre. These results together verified that AAV8-*CreN-InteinN* and AAV *retro-InteinC-CreC* pair is an optimal strategy for circuit-selective *Shank3* gene mutation and visualization.

Finally, we confirmed that Cre expression indeed reduces *Shank3* mRNA level in *Shank3^{f/f}*: *Ai-14* mouse brain by RNA isolation and polymerase chain reaction (PCR) analysis (Figures S1D-S1H; see STAR Methods), which is consistent with a previous report (Wang et al., 2011).

Shank3 mutation alters the morphology of neurons in the PFC-BLA circuit

The circuit-selective Cre expression in the ctMUT mice (*Shank3^{f/f}*: *Ai-14*) visualized tdTomato-positive *Shank3* mutant neurons sparsely in the prelimbic (PL) and infralimbic (IL) areas of the PFC (Figure 1D), which enabled efficient morphological analysis of the circuit neurons using fluorescent microscopy *in vivo*. Confocal z stack images from clarified brain sections containing PFC were 3-dimensionally reconstructed and analyzed in virtual reality (see STAR Methods). The number of primary dendrites was significantly reduced in *Shank3* ctMUT mice (median = 8; 62 neurons from 6 mice) compared with controls (*Ai-14*: median = 10; 39 neurons from 4 mice) (Figures 1H and 1I; Video S1). Analyses of dendritic spines (control: 779 spines from 74 dendritic branches in 4 mice; ctMUT: 1,548 spines from 122 dendritic branches in 6 mice) (Figure 1J) revealed an increase in spine density (control: m = 0.52/μm; ctMUT: median = 0.59/μm) (Figure 1K) as well as decreases in spine length (control: median = 1.37 μm; ctMUT; median = 1.3 μm) (Figure 1L) and spine-head size (control: median = 0.29 μm^2; ctMUT: median = 0.25 μm^2) (Figure 1M) in the ctMUT mice compared with controls. Since the *Shank3* gene was mutated only in the PFC-BLA circuit, these morphological changes are likely caused by the autonomous *Shank3* mutation effect on the circuit neurons, not by the effects from other cells in the brain.

Shank3 ctMUT alters excitatory and inhibitory post-synaptic transmission in the PFC-BLA circuit

Using the circuit gene-manipulation system, we examined the *Shank3* deletion effects on electrophysiological properties in the isolated PFC-BLA circuit neurons. To label ctMUT and WT circuit neurons, *Shank3^{f/f}*: *Ai-14* (ctMUT; n = 10) mice and *Ai-14* (WT; n = 12) mice were injected with AAV8-*CreN-InteinN* and AAV retro-*InteinC-CreC* viruses into the PFC and BLA, respectively (Figure 2A; see STAR Methods). Forty to sixty days following viral injection, whole-cell patch-clamp recording was conducted with the tdTomato-expressing circuit neurons in the brain slices containing the PFC region (Figure

2B). We focused on the PL-BLA circuit neurons since we and another group (Kim et al., 2020; Huang et al., 2020) have shown the importance of the circuit in social behaviors.

Using a voltage-clamp recording, we measured the miniature excitatory post-synaptic current (mEPSC; Figure 2C) and found a significant increase of mean mEPSC amplitude in ctMUT neurons (n = 10 from 3 mice) compared with WT neurons (n = 12 from 3 mice; Figure 2D). The cumulative distribution also showed a significant increase of mEPSC amplitude in ctMUT neurons (Figure 2E). Similarly, ctMUT neurons' mEPSC frequency was significantly increased as shown by mean mEPSC frequency (Figure 2F) and cumulative distribution of inter-event interval (Figure 2G).

On the other hand, the mean amplitude of the miniature inhibitory post-synaptic current (mIPSC; Figure 2H) in circuit neurons (WT: n = 20 from 6 mice; ctMUT: n = 20 from 4 mice) did not show significant changes (Figure 2I). However, the cumulative distribution revealed a significant reduction of mIPSC amplitude in ctMUT neurons compared with WT neurons (Figure 2J). mIPSC frequency in ctMUT neurons was also significantly decreased as shown by both mean mIPSC frequency (Figure 2K) and cumulative distribution of inter-event interval (Figure 2L). Together, these results indicate increased excitatory synaptic transmission and decreased inhibitory synaptic transmission in *Shank3* ctMUT PFC-BLA neurons.

We also tested neuronal excitability and membrane properties using a current-clamp recording by injecting multiple steps of fixed current inputs to the circuit neurons (WT: n = 15 from 3 mice; ctMUT: n = 12 from 3 mice; Figure S3). There was no significant difference in spike frequency in response to the injected currents (Figures S3A and S3B). The mean resting membrane potential (RMP) also showed no significant difference between genotypes (Figure S3C).

Taken together, these electrophysiological findings indicate that *Shank3* ctMUT increases excitatory synaptic input while decreasing inhibitory synaptic input in the PFC-BLA circuit without affecting the neuronal excitability or the RMPs.

Shank3 ctMUT in the PFC-BLA circuit disrupts sociability and alters neural activity

Using the *Shank3* ctMUT mice, we simultaneously monitored the social behaviors and neuronal activity in the PFC-BLA circuit. To enable this approach, we expressed both Cre and Cre-dependent GCaMP7f (Ca^{2+} sensor) in the PFC-BLA circuit (Figure 3A) by injecting a mixture of AAV8-*CreN-InteinN* and AAV9-*Flex-jGCaMP7f* into the PFC and AAV *retro-InteinC-CreC* into the BLA of *Shank3^{f/f}* (ctMUT; n = 10) or WT (control; n = 8) mice. A gradient index (GRIN) lens was implanted over the PL area of PFC to monitor Ca^{2+} signals from the circuit neurons via a miniature microscope (Inscopix) while mice freely moved in a test arena.

In a round social arena (RSA; Figure 3B; see also STAR Methods), a test mouse was allowed to interact with a social stimulus (female C3H/HeJ mouse, p30–p50) inside a transparent inner cage at the center of the arena. One ceiling camera tracked the test animal's entry into a virtual social zone (S-Zone; 3 cm around the inner cage), and another wide-

angle camera installed inside the inner cage provided a 180° view monitoring both animals' detailed social behaviors. Using video clips, the sniffing and reciprocal sniffing (two mice sniffing with their noses toward each other) behaviors were monitored (Video S2). The RSA test with a social stimulus (social stage; Figure 3C) revealed that the *Shank3* ctMUT mice sniffed the social stimulus less in total (Figure 3D), with a shorter mean sniffing duration per bout (Figure 3E), and visited the S-Zone less in total (Figure 3F), with a shorter mean duration per visit (Figure 3G), compared with the WT control group. The ctMUT mice also displayed less reciprocal sniffing (Figure 3H) but a similar mean duration of each event (Figure 3I) compared with the WT controls. Moreover, maximum durations of sniffing (Figure S4B) and S-Zone entry (Figure S4D) were significantly reduced in the ctMUT mice. The maximum duration of reciprocal sniffing in ctMUT mice showed a trend of reduction, but this did not reach statistical significance (Figure S4E). On the other hand, the baseline test with an empty cage (empty stage) did not show any differences between WT and ctMUT mice in any of the behavioral indices, confirming reduced sociability of the *Shank3* ctMUT mice (Figures 3D-3G, S4B, and S4D). There were also no significant differences in traveled distance and mean velocity in all stages (Figures S4F and S4G). All results above were from male test mice because our behavioral analysis did not show significant social deficits in female ctMUT mice (Figures S4I-S4K; see also STAR Methods), which is consistent with the fact that ASD affects females less frequently than males both in human patients and animal models (Fombonne, 2009; Jeon et al., 2018; Matas et al., 2021).

Given that the global *Shank3* knockout mouse lines display various behavioral deficits including anxiety, repetitive behaviors, and motor-coordination defects (Peça et al., 2011; Wang et al., 2011), we tested the *Shank3* ctMUT mice with open-field (motor activity and anxiety) (Figures S4L-S4P), grooming and marble burying (repetitive behavior) (Figures S4Q-S4S and S4Y), light-dark box (anxiety) (Figures S4V-S4X), rotarod (motor coordination) (Figures S4Za and S4Zb), and fear-conditioning (Figure S7) tests. However, no significant behavioral differences between WT and ctMUT mice were found in these tests, suggesting that the effects of *Shank3* ctMUT in the PFC-BLA circuit are likely to be confined to social behaviors.

Ca^{2+} imaging in PFC-BLA circuit neurons revealed abnormal neural activities in the *Shank3* ctMUT mice (Figure 3J; Video S2) which is in line with our electrophysiology results and previous reports (Yoo et al., 2019; Chen et al., 2020). During both empty and social tests, Ca^{2+} signal amplitude and amplitude variance were significantly increased in the ctMUT neurons compared with those of the WT neurons (Figures 3K and 3L). Similar effects were also observed in the open-field (Figures S4T and S4U) and fear-conditioning (Figures S7C and S7D) tests, indicating that the basal activity and variability of the PFC-BLA circuit neurons are enhanced by *Shank3* ctMUT. Note that there was no group difference in the background fluorescence during Ca^{2+} imaging (Figure S4H). Interestingly, the variance of amplitude in Ca^{2+} transient is positively correlated with the amplitude of Ca^{2+} transient (Figure 3M), suggesting that the hyper-amplitude and -variability of *Shank3* ctMUT neurons could be a coexisting cellular pathology for abnormal social behaviors in these mice. These findings inspired us to analyze whether functional connectivity between the PFC and BLA is also increased in human individuals with ASD.

Human ASD individuals display hyper-connectivity with increased functional connectivity variability between the mPFC and the amygdala

We analyzed the resting-state functional magnetic resonance imaging (rs-fMRI) data from ASD and the control (typical development individuals) that were obtained from the Autism Brain Imaging Data Exchange (ABIDE) dataset (Di Martino et al., 2014) (Figures 4A and 4B; see STAR Methods). Given the resolution limitation in human imaging data, we focused our analyses on the medial PFC (mPFC) and amygdala regions as a proxy of PFC and BLA in the mouse brain. We discovered that individuals with ASD showed a higher mPFC-amygdala functional connectivity than control for both static (static-FC; Figure 4C) and dynamic (dynamic-FC; Figure 4D) levels. To confirm that the hyper-connectivity pattern is specific to the mPFC-amygdala circuit in ASD, we also examined pairwise functional connectivity of the mPFC with other regions such as post-central, orbitofrontal cortex (OFC), and dorsolateral PFC (DLPFC). Two-way repeated-measures ANOVAs revealed significant main effects of the regions and the group, but interaction effects were not significant. This is because mPFC-OFC and mPFC-DLPFC connectivity were slightly elevated in ASD, but they were not significantly different between the groups. The additional independent t tests supported the specificity of mPFC-amygdala connectivity difference between groups (Figures 4C and 4D; see Tables S1A, S1B, and S1E for statistical details). Consistent with the findings from the *Shank3* ctMUT mouse model, an additional functional connectivity variability analysis between the mPFC and amygdala by mean square successive difference (MSSD) revealed that ASD individuals showed a hyper-variant connection compared with control individuals (Figure 4E). However, the connectivity variabilities paired with the control region were not significantly different between the groups. In the two-way ANOVAs, the interaction effects were not significant, but the main effects of the regions were significant (see Tables S1C and S1E for statistical details). These results suggest that the hyper-connectivity and -variability pattern of mPFC-amygdala in ASD was more significant than that of mPFC-control regions. Finally, machinelearning-based group classification analysis revealed significantly higher accuracy than chance level in identifying ASD from healthy individuals based on the dynamic mPFC-amygdala connectivity patterns, whereas the other control circuits did not (Figure 4F; see Tables S1D and S1E for statistical details). These findings suggest that the PFC-BLA circuit hyper-activity and -variability are not only confined to the *Shank3* ctMUT mouse model but may be one of the major neural features underlying human ASD as well.

Shank3 ctMUT reduces the temporal correlation of the PFC-BLA circuit activity with social behaviors

How do the hyper-activity and -variability of the ctMUT neurons affect the PFC-BLA circuit function associated with social behaviors? To address this question, we first clarified the subjects of analyses by classifying the behaviorally tuned neurons (neurons showing social-behavior-specific increase or decrease in activities) using a similarity comparison method (Carrillo-Reid et al., 2015; Hamm et al., 2017; Liang et al., 2018). We calculated the correlative relationship between a neuron's Ca^{2+} trace and a behavior vector and confirmed its statistical significance (Figures 5B and S5A; see STAR Methods). Three subclasses of social behaviors were subjected to analyses: S-Zone entry, sniffing, and reciprocal sniffing. The neurons displaying significant similarities to each social behavior were assigned as

"ON" and significant dissimilarities as "OFF" (Figures 5B-5D, S5C, S5D, S5N, and S5O; see Figures S5A and STAR Methods for detailed criteria). Neurons that were neither ON nor OFF were assigned as "Other". Population analysis of all neurons (WT: n = 675 from 8 mice, ctMUT: n = 1,112 from 10 mice) revealed that 12% (n = 81) and 13.48% (n = 91) of WT circuit neurons were classified as social-ON and -OFF (ON or OFF to at least one social behavior) neurons, respectively, while 7.73% (n = 86) and 9.53% (n = 106) of ctMUT circuit neurons were social-ON and -OFF neurons, respectively (Figures S5X and S5Y). The remaining neurons that were neither social-ON nor -OFF were assigned as "True Other" (WT: 74.51% [n = 503], ctMUT: 82.73% [n = 920]), which were Other to all social behaviors (Figures S5X and S5Y). We also tested whether behaviorally tuned neurons for sniffing and S-Zone entry in the empty stage overlap with the neurons tuned in the social stage, and found that only 16.91% (n = 35) and 10.84% (n = 27) of behaviorally tuned neurons overlap across stages, respectively (Figures S5Za and S5Zb), indicating that most of the behaviorally tuned neurons for social stimulus are different from the ones that are tuned in the absence of social stimulus.

To determine the relationship between neural activity and social behavior, the correlation between Ca^{2+} transients and social-behavior vectors for each group of ON, OFF, and Other neurons was analyzed. The data revealed that both ctMUT ON and OFF neurons showed a significantly lower correlation between Ca^{2+} transients and social behaviors including sniffing (Figures 5E and 5I), S-Zone entry (Figures S5E and S5I), and reciprocal sniffing (Figures S5P and S5T) compared with WT counterpart neurons, indicating that the temporal correlation between the PFC-BLA circuit activity and social behaviors is disrupted by the *Shank3* ctMUT. Further analyses revealed significantly larger amplitudes and increased amplitude variances in ctMUT sniffing-ON and -OFF (Figures 5F, 5G, 5J, and 5K), S-Zone-ON and -OFF (Figures S5F, S5G, S5J, and S5K), and reciprocal sniffing-ON neurons (Figures S5Q and S5R). Moreover, the similarity between Ca^{2+} transient and sniffing behavior was negatively correlated with the amplitude and amplitude variances (Figures 5H and 5L) in ON and OFF neurons not only in ctMUT but also in WT mice. Similar negative correlations were also observed in S-Zone-ON/OFF and reciprocal sniffing-ON neurons of WT and ctMUT mice (Figures S5H, S5L, S5S, and S5W) but not in reciprocal sniffing-OFF neurons (Figure S5W), presumably due to a floor effect, as ctMUT reciprocal sniffing-OFF neurons displayed the lowest similarity values compared with other neurons (Figure S5T). Together, these data suggest that *Shank3* ctMUT induces circuit hyper-activity and -variability that could interrupt the temporal correlation between neural activity and social behaviors.

To examine whether the *Shank3* in the PFC-BLA circuit serves specifically for social behavior, we analyzed the neural responses during other behaviors including grooming, rearing, and climbing in the S-Zone (Figure S6A). In this analysis, WT and *Shank3* ctMUT mice showed similar levels of rearing and climbing behaviors (Figure S6C). The temporal correlation of circuit neural responses with rearing and climbing behaviors in the S-Zone were not significantly changed by *Shank3* ctMUT (Figures S6E-S6H). These data support the hypothesis that *Shank3* in the PFC-BLA circuit may largely contribute to social behavior. Analysis for grooming was not feasible because mice did not groom in the S-Zone (Figure S6B).

We also tested whether the circuit neural response to the sniffing on the young C3H mouse is a social response or just a simple response induced by olfactory exploration. Indeed, sniffing-ON and -OFF neurons identified during social stage showed an extremely low temporal correlation with the empty-cage-sniffing behavior (sniffing toward an empty cage) (Figures S6I-S6N). Moreover, an additional non-social olfaction test utilizing two types of tactile objects also revealed similar results (Figures S6O-S6T). These data together suggest that the neural response of the sniffing-ON and -OFF neurons to the C3H mouse may not be a simple response induced by olfaction but is likely a social neural response.

The social deficit displayed by *Shank3* ctMUT mice could be a manifestation of an abnormality in fear learning. To address this issue, using the fear-conditioning paradigm, we examined freezing behavior as an index of fear learning and memory as well as analyzed the neural responses during fear conditioning and following cued memory test (Figure S7A; Video S2). WT and ctMUT mice showed a similar level of freezing behavior during both conditioning and test phases (Figure S7B), suggesting that *Shank3* ctMUT did not affect fear learning and memory. Neural response analyses revealed overall increased Ca^{2+} transient amplitude and variance in ctMUT mice compared with those of WT mice (Figures S7C and S7D) as observed in all other behavioral tests. We next selected unconditional stimulus (US; footshock)-responsive and conditional stimulus (CS; tone)-responsive neurons (see STAR Methods) and analyzed Ca^{2+} transients during conditioning and test phases. Results showed that normalized Ca^{2+} transients were not different between each genotype during conditioning (Figure S7E) as well as in test phases (Figure S7F). These results suggest that *Shank3* ctMUT effects on social behavior and neural responses to the social behavior may not be attributable to change in fear response or learning of fear.

Shank3 ctMUT enhances neural activity proportional to the duration of social behavior

Is the variability in Ca^{2+} transients random or related to social behaviors? Why is the amplitude variance of the *Shank3* ctMUT higher than that of the WT? To answer these questions, we analyzed the relationship between a maximum normalized peak amplitude of sniffing-ON neurons and the duration of the sniffing bout in which the peak occurred, revealing that they are positively correlated with each other in both WT and ctMUT groups (Figure 6A). Importantly, sniffing-ON neurons of ctMUT showed a higher correlation coefficient than those of WT mice (Figure 6A). Similar results were found in S-Zone entry (Figure S8A) and reciprocal sniffing (Figure S8B). These results suggest that the amplitude of neural activity is not random but proportional to the duration of social behavior, which is enhanced by *Shank3* ctMUT.

To reveal the *Shank3* ctMUT effect on the hyper-correlation between Ca^{2+} transients and the duration of social behavior, we separated social behaviors into various time windows according to the time span in each social-behavior epoch (<1, 1–3, 3–5, 5–7, and >7 s) (Figures 6B and S8C) and monitored Ca^{2+} transient dynamics during these time segments aligned to the onset of the social behaviors (Figures 6C, 6D, S8D, and S8E). The sniffing-ON neurons' mean normalized Ca^{2+} transients (normalized F/F) in both groups showed a pattern of increased amplitude proportionally to the length of the sniffing duration, which was even more increased in ctMUT sniffing-ON neurons (Figure 6C). The analysis in the

first 2 s of the sniffing revealed that WT sniffing-ON neurons' mean normalized ΔF/F significantly increased until the medium-length window (3–5 s) and was slightly decreased in the longest windows (>7 s) (Figure 6D). On the other hand, the ctMUT sniffing-ON neurons' normalized ΔF/F continued to increase even in the longer windows (5–7 and >7 s) (Figure 6D). When these neurons were analyzed during sniffing on an empty stage, no significant difference between genotypes was observed (Figures S6M and S6N).

To verify whether these results were confined to behavioral epochs, we conducted a random sampling of 4 s windows 5,000 times and observed that all neurons' normalized ΔF/F were flattened to zero (Figures S8F and S8G). Together, these results suggest that *Shank3* mutation in the PFC-BLA circuit exacerbates the social-ON neuron's circuit response proportionally to the duration of social interactions, resulting in hyper-variability of circuit activity in the ctMUT neurons. Similar results were found in S-Zone-ON neurons (Figures S8D and S8E), but the same analysis could not be applied to the reciprocal sniffing-ON neurons due to a limited number of trials. Also, ctMUT social-OFF neurons could not be analyzed with the same methods due to the lack of Ca^{2+} transients during behavior epochs.

Social deficit of *Shank3* ctMUT mice is mimicked by optogenetic circuit activation and partially rescued by circuit inactivation

Based on the results above, we hypothesized that the hyperactivity of the ctMUT neurons (Figure 3), especially for the social-ON neurons' hyper-activity during social behaviors (Figure 6), could be a major factor driving social dysfunction. To test this hypothesis, we mimicked the *Shank3* ctMUT neurons by conditional activation of the PFC-BLA circuit neurons during social interaction in RSA. We selectively expressed channelrhodopsin 2 (ChR2) in the PFC-BLA circuit by transducing the mixture of AAV8-*CreN-InteinN/AAV8-Flex-ChR2-EYFP* and AAV retro-*InteinC-CreC* into the PFC and BLA, respectively (Figure 7A). For control, the same viruses except for the AAV8-*Flex-ChR2-EYFP* were injected (opsin-free). Two weeks after viral injection, optic fibers were implanted bilaterally into the PFC, and an RSA social test was conducted 2 weeks after the implantations. Mice were tested by empty RSA, baseline social RSA, and social RSA with 5 Hz optic stimulations (473 nm, ~5 mW) for 3 consecutive days (Figure 7B; Video S3). The optical stimulations were conditionally delivered only when the test mice entered the S-Zone and ceased when mice went out of the S-zone.

In this test, the mean and maximum durations of sniffing were significantly reduced by the optic stimulation (Figures 7D and 7E), but total sniffing duration was not affected (Figure 7C). In the S-Zone entry, the optic stimulation reduced the maximum durations in the S-Zone (Figure 7H) but did not alter the total and mean duration of S-Zone entry (Figures 7F and 7G). Regarding reciprocal sniffing, the mean duration of reciprocal-sniffing behavior was significantly decreased (Figure 7J). The total and maximum duration showed reduced tendencies but did not reach statistical significance (Figures 7I and 7K). However, the same optic stimulation in the opsin-free group did not show any alterations in all the indices of behaviors (Figures 7C-7K). Finally, the same optogenetic activation in absence of social stimulus did not reduce total, mean, and maximum durations of sniffing on the inner cage, suggesting that the circuit-activation-induced loss of sociability may not be

attributable to the aversion response to the optic activation (Figures S9A-S9I). Together, these results demonstrate that hyperactivity of PFC-BLA circuit neurons can disrupt stable social interactions.

Next, we conducted optogenetic silencing with *Shank3* ctMUT mice (Figures S9J-S9V). Using *Shank3^f/f* mice, we selectively expressed Archaerhodopsin (eArch3.0) (Mattis et al., 2012) in the PFC-BLA circuit by transducing the mixture of AAV8-*CreN-InteinN/AAV DJ-Flex-EF1α-eArch3.0-EYFP* and AAV retro-*InteinC-CreC* into the PFC and BLA, respectively (ctMUT-eArch3.0; n = 8; Figure S9J). For control, the same viruses except for the AAV *DJ-Flex-EF1α-eArch3.0-EYFP* were injected in the *Shank3^f/f* mice (ctMUT opsin-free; n = 6). To conditionally silence the circuit neurons, light stimulation (520 nm, ~11 mW, constant during stimulation) was given when a mouse entered the S-Zone (Figure S9K; Video S3).

As a result, conditional inhibition of the ctMUT circuit neurons with eArch3.0 increased total sniffing duration (Figure S9L, left), mean sniffing duration per bout (Figure S9M, left), and total S-Zone-entry duration (Figure S9O, left) compared with baseline, whereas the opsin-free group showed no effect. The comparison of the increased amount of these social behaviors between groups, however, showed no statistical significance, albeit showing higher mean values for the eArch3.0 group (Figures S9L, right, S9M, right, and S9O, right). Moreover, other indices such as maximum sniffing duration per bout (Figure S9N), mean S-Zone-entry duration (Figure S9P), maximum S-Zone-entry duration per visit (Figure S9Q), and all indices of reciprocal sniffing (Figures S9R and S9T) were not affected. These results suggest that optogenetically induced rescue effects might be limited to the subset of social behaviors.

To verify whether optogenetic-inhibition effects were not from non-social effects such as place preference, mice were tested in open field with conditional optogenetic inhibition given when they entered the center region of the arena (Figure S9U). The results confirmed that both eArch3.0 and opsin-free groups showed similar levels of exploration in the center area (Figure S9V), indicating that the optogenetic-rescue effects may not be due to the preference for the center area.

These results demonstrate that conditional inactivation of the ctMUT PFC-BLA circuit can partially rescue some of the social behaviors. This limited rescue effect may be due to the nature of optogenetic silencing that wipes out the circuit activities instead of restoring the neural activities to the normal range.

DISCUSSION

To date, polymorphisms in many genes have been attributed to neuropsychiatric disorders. However, in many cases, the candidate gene approach using animal models with global gene manipulations often failed to provide clear mechanistic insights into disorders due to the extremely complex nature of the brain. This limitation led us to isolate a neural circuit and focus on interregional neural connectivity. The circuit-level genetic approach requires precise gene-manipulation technology acting exclusively within an isolated target circuit. In

this study, we exploited a highly specific and robust circuit-selective Cre-expressing strategy that not only mutates the *Shank3* gene but also expresses transgenes such as GCaMP7f, ChR2, and eArch3.0 in the unidirectional PFC-BLA circuit. In future work, it will be important to address how the recipient cells in the BLA respond to the PFC-BLA circuit activity during social behaviors. This expansion to the second node of this network could be achieved by selective labeling of the recipient neurons in the BLA. The modification of our strategy replacing the AAV8 with the AAV9 serotype, as shown in Figure S2G, would be a useful tool for the approach.

Previous studies using *Shank3* mutant mice reported varied, sometimes even contrary, results on morphological and electrophysiological properties depending upon the brain regions subjected to analyses (Yoo et al., 2019; Wang et al., 2016; Yi et al., 2016; Bozdagi et al., 2010), suggesting that the *Shank3*-deletion effects may be determined by the cell types and regional characteristics. In our previous studies, we demonstrated that the deletion of *ArpC3*, an important cytoskeletal regulator, in the PFC-BLA circuit leads to immature dendritic spines that form abnormal synaptic contacts with afferent axon terminals, resulting in increased excitatory post-synaptic transmission and decreased inhibitory post-synaptic transmission as well as social dysfunction (Kim et al., 2015a, 2020). Interestingly, *Shank3* ctMUT mice also exhibited abnormal dendritic-spine morphology in the PFC-BLA circuit as well as displayed abnormal electrophysiological properties and social dysfunction. These data from two different mouse models suggest that within PFC-BLA circuit neurons, spine maturation may be the key factor for maintaining a normal level of neural activity and social behaviors.

Our electrophysiological analyses revealed that *Shank3* ctMUT alters only the post-synaptic input properties but not the neuronal excitability and RMP. Thus, the increased neural-circuit activity indicated by the increased Ca^{2+} transients may be attributable to the abnormal post-synaptic input. These functional characteristics may be specific to PFC-BLA circuit neurons, as *Shank3* deletion in striatal or hippocampal neurons showed different results (Wang et al., 2016; Yi et al., 2016).

We demonstrated the existence of socially tuned neurons in the PFC-BLA circuit that specifically and differentially responded to multiple classes of social behaviors. Thus, we hypothesized that each social behavior can be conversely predicted by the patterns of neural-circuit activities. To address this hypothesis, we conducted decoding analyses using ensembles of Ca^{2+} traces. Data revealed that a population of PFC-BLA circuit neurons encode multiple social behaviors via non-linear ensemble patterns (Figures S10A-S10K; STAR Methods) similar to evidence from PFC neurons (Frost et al., 2021). Network analysis revealed that PFC-BLA circuit neurons form a functional network in which a small population of ctMUT social-responsive neurons has a stronger influence on the rest of the circuit neurons than WT (Figures S10L-S10X; STAR Methods). These results suggest that *Shank3* ctMUT effects are not only limited to social-ON neurons, which have a direct and linear relationship to social behaviors, but may have a strong indirect influence on the network of other circuit neurons, which are non-linearly involved in social behaviors. All the machine-learning and network analyses can be found in Figure S10 and STAR Methods. However, precise mechanisms underlying this intra-circuit network function remain to be

further investigated in future studies with advanced circuit-manipulation technology and analyses.

The neural-circuit abnormalities observed in the *Shank3* ctMUT mice are supported by the neuroimaging results from human ASD patients at both static and dynamic levels. Similar hyper-connectivity of ASD patients was previously reported (Uddin et al., 2013; Harlalka et al., 2019; Li et al., 2020; Lynch et al., 2013; Supekar et al., 2013) as well as hyper-variant connectivity patterns (Harlalka et al., 2019). Moreover, theoretical and empirical studies have emphasized the role of mPFC and amygdala in social behaviors, as these two regions are involved in reciprocal social processes such as mediating eye gaze to others and emotion recognition from others' faces (Fried et al., 1997; Hoehl et al., 2009). Consistent with findings of the PFC-BLA hyper-activity and -variability of *Shank3* ctMUT mice during the emptystage condition of RSA and the open-field test (i.e., non-social- and -task-related phases), we found similar abnormalities in the ASD patients during the resting state.

In addition, we attempted to establish the causal relationship between circuit hyperactivity and social dysfunction using optogenetics. Previous studies reported that optogenetic activation of PFC neurons can disrupt social behavior (Yizhar et al., 2011), and we also demonstrated that activation of PFC-BLA circuit neurons can impair social preference during a social-affiliation test (Kim et al., 2020). As our RSA test provides more detailed analytic measures on social behaviors such as sniffing and reciprocal sniffing, we observed that optogenetic activation of the WT circuit neurons partially emulates the social dysfunction of ctMUT mice, and optogenetic inhibition of the ctMUT neurons rescue only some of the disrupted social behaviors. These incomplete recapitulation and rescue effects may be due to an artificial manipulation pattern that either activates or silences the entire circuit neurons simultaneously, neglecting functional differences in the individual circuit neurons.

Finally, it should be noted that only male mice were used due to the male bias in social behavioral deficits. Our pilot study using female *Shank3* ctMUT mice did not show significant social deficits. This sex difference in prevalence has been consistently observed in human patients and ASD mouse models (Fombonne, 2009; Jeon et al., 2018; Matas et al., 2021). Hormonal or genetic factors have been attributed to the sex difference (Werling and Geschwind, 2013; Berkel et al., 2018), but the exact mechanism remains to be elucidated.

Taken together, the results of the present study reveal how genetic mutation of ASD-risk *Shank3* within a specific neural circuit can affect neuronal signaling and functional connectivity and contribute to impaired social behavior. Our circuit-specific approach promises to identify more precisely the neural mechanisms underlying specific behavioral abnormalities relevant to ASD symptoms.

Limitations of the study

The current study utilized *in vivo* Ca^{2+} imaging to monitor neural activity during behavior. As Ca^{2+} is an indirect measurement of the electrophysiological activity of the neurons, the possibility of unknown effects from genetic mutations that alter Ca^{2+} levels independent of the neuronal response cannot be completely ruled out. It should also be noted that the

optogenetic strategy is not an exact recapitulation of *Shank3* ctMUT neurons, as optogenetic stimulation is an artificial manipulation that activates all circuit neurons simultaneously regardless of each neuron's functional characteristics and network dynamics between multiple neurons. Finally, we found a similar circuit abnormality in our mouse model and human patients. Yet, caution is needed when comparing cross-species results given the differences in signal characteristics between blood-oxygen-level-dependent (BOLD; i.e., oxygen changes) in human imaging and Ca^{2+} imaging of single neurons in mice. It would be reasonable to conclude that both human and animal studies consistently indicate that abnormalities in signaling between the PFC and BLA can be associated with social dysfunction.

STAR★METHODS

RESOURCE AVAILABILITY

Lead contact—Further information and requests for resources and reagents should be directed to and will be fulfilled by the Lead Contact, Il Hwan Kim (ikim9@uthsc.edu).

Materials availability—All materials and reagents developed in this study will be available from the Lead contact upon request.

Data and code availability

- All data reported in this study will be available from the Lead contact upon request.

- Original code for Round social arena has been deposited at Zenodo and is publicly available as of the date of publication. DOIs are listed in the Key resources table.

- Any additional information required to reanalyze the data reported in this paper is available from the Lead contact upon request.

EXPERIMENTAL MODEL AND SUBJECT DETAILS

Animals—*Shank3*[f/f (e4-9)] line was described in the previous report (Wang et al., 2011). *Ai-14* (B6; 129S6-Gt(ROSA)26Sor[tm14(CAG-tdTomato)Hze]/J; stock no. 007908), C3H/HeJ (stock no. 000659; female, 4 weeks), and C57BL/6J (stock no. 000664; male and female, 8 weeks) mice were purchased from Jackson Laboratory. The genetic background of all transgenic mice used in the current study was 129Sv × C57BL/6J. All mice were housed (normally 3–4 mice per cage, test mice were isolated in a single-housing cage 1 week before the social experiment) in the Laboratory Animal Care Unit (LACU) of the University of Tennessee Health Science Center. Surgeries were conducted when subject mice were around 9–11 week old and behavioral tests were conducted when mice are 3–5 months old. All tests were conducted during the light cycle. All procedures were conducted with a protocol approved by the University of Tennessee Institutional Animal Care and Use Committee in accordance with US National Institutes of Health guidelines.

METHOD DETAILS

AAV preparation—For the production of AAV-*CreN-InteinN* and AAV-*InteinC-CreC*, the *CreN-InteinN* and *InteinC-CreC* sequences (generously provided by Dr. Fan Wang) (Wang et al., 2012) were inserted into vector backbone pAAV-EF1α (Kim et al., 2015a, 2020). AAV2/8-*Ef1α-CreN-InteinN* (AAV8-*CreN-InteinN*), AAV2/9-*Ef1α-CreN-InteinN* (AAV9-*CreN-InteinN*), Retrograde AAV-*Ef1α-InteinC-CreC* (AAV retro-*InteinC-CreC*), Retrograde AAV-*Ef1α-CreN-InteinN* (AAV retro-*CreN-InteinN*), AAV2/9-*hSyn-Cre* (AAV9-*Cre*), AAV2/8-*Ef1α-Flex-GFP* (AAV8-*Flex-GFP*) (Kim et al., 2015a), and AAV2/8-*Ef1α-Flex-ChR2-EYFP* (AAV8-*Flex-ChR2-EYFP*) (Addgene 20298) were purified as described in previous reports (Kim et al., 2015a, 2020). Each AAV vector was co-transfected with the packaging plasmid serotype 2/8 (Addgene 112864), 2/9 (Addgene 112865), or retrograde AAV (Addgene 81070), and pAd-deltaF helper plasmids (Addgene 112867) into HEK293T cells using the PEI method. After 48 h incubation, cells were collected, lysed by three times of freeze-thaw cycles in lysis buffer (150 mM NaCl, 20 mM Tris-HCl; pH 8.5), and incubated with benzonase (50 U/mL; Novagen) for 30 min in 37°C. The viral particles were then concentrated by ultracentrifugation ($67,000 \times g$, 1 h) using an iodixanol gradient solution (Optiprep; 15%, 25%, 40%, and 60%), and purified 3 times using an Amicon filter unit (100K MWCO; Millipore) by exchanging into PBS. The titer of each AAV was measured by real-time PCR (IQ5; BioRad) targeting WPRE sequence. pGP-AAV2/9-*Syn-Flex-jGCaMP7f-WPRE* (AAV9-*Flex-jGCaMP7f*; Dana et al., 2019) was purchased from Addgene (Addgene 104492-AAV9). AAV *DJ-Flex-EF1α-eArch3.0-EYFP* (GVVC-AAV-55) was purchased from Stanford vector core.

Cell biology—HEK293T cells were seeded onto 24 wells plate (5×10^{14} cells/well) and 1 mL of one or more viral vectors were treated onto the well, depending on the treatment conditions. Viral titrations were as follows: AAV8-*CreN-InteinN* (5.1×10^{13} GC/mL), AAV retro-*InteinC-CreC* (1.1×10^{13} GC/mL), and AAV8-*Flex-GFP* (2.2×10^{13} GC/mL). After 3 days of incubation at 37°C, 4′,6-diamidino-2-phenylindole solution (DAPI; Sigma-Aldrich; diluted to 1/10,000) was treated to each well. Then the wells were imaged with a CELENA-S Digital Imaging System Microscope (Logos Biosystem) with a 20× objective.

Stereotaxic surgeries for viral injections—Stereotaxic surgeries for viral injections were performed as described in our previous reports (Kim et al., 2013, 2015a, 2020). In brief, mice (9–11 week old) were kept in deep anesthetization using an isoflurane vaporizer (VetEquip) connected with a gas head holder (David Kopf Instruments) while fixed in a stereotaxic frame (David Kopf Instruments). All viruses were infused into the brain regions for at least 15 to 20 min using a Nanoject II (Drummond Scientific Company) connected to a glass micropipette, targeting the PFC (AP: +2.5, ML ±1.0, DV: −0.5 to −1.5 from brain surface) or BLA (AP: −1.8, ML ± 3.3, DV: −4 to −4.3 from brain surface). The injection pipette was left in place for at least 5 min post-injection before it was retracted.

Surgery for the PFC-BLA circuit tracing: *Ai-14* (Cre-reporter tdTomato) male mice and *Shank3^f/f(* e4-9): *Ai-14* double mutant male mice were used for testing circuit-selective Cre expression. AAV8-*CreN-InteinN* (300 nL; 5.1×10^{13} GC/mL) and AAV retro-*InteinC-CreC* (200 nL; 1.1×10^{13} GC/mL) were injected into the PFC (AP: +2.5, ML ±1.0, DV: −0.5 to

−1.5 from brain surface) and BLA (AP: −1.8, ML ±3.3, DV: −4 to −4.3 from brain surface), respectively.

Surgery for tracing all PFC projections: For testing conventional region-specific Cre expression in PFC neurons, AAV9-Cre (300 nL; 2.7×10^{13} GC/mL) was injected into the PFC (AP: +2.5, ML ±1.0, DV: −0.5 to −1.5 from brain surface) of *Ai-14* male mice.

Surgery for testing AAV9 serotype: As AAV9 serotype has been reported to show transsynaptic translocation in the recipient cells (Zingg et al., 2017), we tested this possibility by injecting AAV9-*InteinN-CreN* (150 nL; 5.1×10^{13} GC/mL) and AAV retro-*InteinC-CreC* (50 nL; 1.1×10^{13} GC/mL) into the PFC (AP: +2.5, ML ±1.0, DV: −0.5 to −1.5 from brain surface) and BLA (AP: −1.8, ML ±3.3, DV: −4 to −4.3 from brain surface) of *Ai-14* male mice, respectively.

Surgery for conventional retrograde tracing: To compare split-Cre system to conventional retrograde tracing, Cholera toxin subunit B conjugated with Alexa Fluor 488 (CTB, 150nL, 0.5% in PBS) was mixed with AAV retro-*InteinC-CreC* (150 nL; 4.7×10^{13} GC/mL) and injected into BLA (AP: −1.8, ML ±3.3, DV: −4 to −4.3 from brain surface) of *Ai-14* male mice (n = 3). Separately, AAV8-*CreN-InteinN* (300 nL; 1.3×10^{13} GC/mL) was injected into the PFC (AP: +2.5, ML ±1.0, DV: −0.5 to −1.5 from brain surface).

***Surgery for testing deletion of* Shank3 *mRNA*:** To verify Cre expression in the *Shank3^{f/f (e4-9)}*): *Ai-14* mice indeed deletes *Shank3* mRNA, AAV9-*Cre* was injected into the unilateral hemisphere (right) of the brain in the PFC region (AP: +2.5, ML ±1.0, DV: −0.5 to −1.5 from brain surface). In the left hemisphere, AAV9-*GFP* was injected as a control. Three male *Shank3 ^{f/f (e4-9)}*): *Ai-14* mice were used for viral injection.

Surgery for whole-cell patch clamp recording: *Ai-14* (Cre-reporter tdTomato) male mice (WT: n = 12) and *Shank3^{f/f (e4-9)}*: *Ai-14* double mutant male mice (ctMUT: n = 10) were used whole-cell patch clamp recording. AAV8-*CreN-InteinN* (300 nL; 5.1×10^{13} GC/mL) and AAV retro-*InteinC-CreC* (200 nL; 1.1×10^{13} GC/mL) were injected into the PFC (AP: +2.5, ML ± 1.0, DV: −0.5 to −1.5 from brain surface) and BLA (AP: −1.8, ML ± 3.3, DV: −4 to −4.3 from brain surface), respectively. For voltage-clamp recording of miniature excitatory postsynaptic current (mEPSC), 3 WT mice and 3 ctMUT mice were used. For voltage-clamp recording of miniature inhibitory postsynaptic current (mIPSC), 6 WT mice and 4 ctMUT mice were used. For current clamp recording, 3 WT mice and 3 ctMUT mice were used.

***Surgery for simultaneous* Shank3 *ctMUT and Ca^{2+} imaging*:** For simultaneous circuit-specific expression of genetically encoded calcium indicator GCaMP7f and circuit-selective mutation of *Shank3* exons 4–9 within the PFC-BLA circuit, a mixture of AAV8-*CreN-InteinN* (250 nL; 5.1×10^{13} GC/mL) and AAV9-*Flex-jGCaMP7f* (250 nL; 1×10^{13} GC/mL) was slowly injected into the PFC (AP: +2.5, ML ±0.5, DV: −0.5 to −1.5 from brain surface), and AAV retro-*InteinC-CreC* (200 nL; 1.1×10^{13} GC/mL) was injected into the BLA (AP: −1.8, ML ±3.3, DV: −4 to −4.3 from brain surface), of the *Shank3^{f/f (e4-9)}* mice (male, n =

10) creating a circuit-selective-mutant group (ctMUT). Control littermate WT mice received the same viral injections (male, n = 8).

Surgery for PFC-BLA ChR2 circuit-selective knockin (ctKI): For circuit-specific expression of ChR2 within the PFC-BLA circuit, a mixture of AAV8-*CreN-InteinN* (250 nL; 5.1×10^{13} GC/mL) and AAV8-*Flex-ChR2-EYFP* (250 nL; 1.3×10^{13} GC/mL) was slowly injected into the PFC (AP: +2.5, ML ± 0.5, DV: −0.5 to −1.5 from brain surface), and AAV retro-*InteinC-CreC* (200 nL; 1.1×10^{13} GC/mL) was injected into the BLA (AP: −1.8, ML ± 3.3, DV: −4 to −4.3 from brain surface) (ChR2-ctKI group). In the control group (Opsin-free), the same viruses except for AAV8-*Flex-ChR2-EYFP* were injected into the PFC and BLA. Wild type C57BL/6J mice were used for both Opsin-free (male, n = 6) and ctKI (male, n = 6) groups.

***Surgery for PFC-BLA* eArch3.0 *circuit-selective knockin (ctKI) for ctMUT mice*:** For circuit-specific expression of eArch3.0 within the PFC-BLA circuit of ctMUT mice, a mixture of AAV8-*CreN-InteinN* (300 nL; 1.3×10^{13} GC/mL) and AAV *DJ-Flex-EF1a-eArch3.0-EYFP* (300 nL; 1×10^{13} GC/mL) was slowly injected into the PFC (AP: +2.5, ML ±0.5, DV: −0.5 to −1.5 from brain surface), and AAV retro-*InteinC-CreC* (200 nL; 4.7×10^{13} GC/mL) was injected into the BLA (AP: −1.8, ML ±3.3, DV: −4 to −4.3 from brain surface) (ctMUT-eArch3.0 group). In the control group (ctMUT-Opsin free), the same viruses except for AAV *DJ-Flex-EF1a-eArch3.0-EYFP* were injected into the PFC and BLA. *Shank3* $^{f/f}$ mice were used for both ctMUT-Opsin free (male, n = 6) and ctMUT-eArch3.0 (male, n = 8) groups.

Circuit tracing—The circuit tracing procedure was conducted as described in our previous studies (Kim et al., 2015a, 2020). Two weeks after the AAV infections (and CTB injection), mice were deeply anesthetized with isoflurane and were perfused transcardially with phosphate-buffered saline (PBS) containing 25 U/mL heparin, followed by 4% PFA in PBS. Perfused brains were removed, post-fixed overnight at 4°C in 4% PFA, and then were cryo-protected with 30% sucrose in PBS. Brains were cut into 50 mm coronal sections by cryostat (Leica CM 1950). Sections were washed with PBST (PBS containing 0.2% Triton X-100) for 15 min, then were stained with a 4′,6-diamidino-2-phenylindole solution (DAPI; Sigma-Aldrich). After washing three times with PBST, the serial sections were cover-slipped with ProLong Glass (Invitrogen) anti-fade mounting medium. Images were taken by tile scan imaging using an LSM 710 confocal microscope (Zeiss) with 10× and 20× objectives under the control of Zen software (Zeiss). To obtain a detailed view of cell bodies and axonal fibers, 63× oil-immersion objective lens was used.

Cell and spine morphology—Four weeks after viral injection, the *Shank3* $^{f/f}$ (e4-9): *Ai-14* double mutant mice (ctMUT, n = 6) and *Ai-14* mice (control, n = 4) were perfused and their brains were cleared using an SHIELD protocol (Park et al., 2019). In detail, we perfused and preserved mice brains using SHIELD solutions (LifeCanvas technologies) to protect Cre-reporting tdTomato signals, and the brains were cut into 100 μm coronal sections by vibratome. Then the brain sections were cleared with Smart Clear Pro II (LifeCanvas technologies) and were washed in PBS. After washing, the refractive index was matched

with an optical clearing solution and the sections were then cover-slipped with the same optical clearing solution. Images were taken by z stack imaging (0.13 μm/step) using an LSM 710 confocal microscope (Zeiss) with a 20× objective lens and 63× oil-immersion objective lens under the control of Zen software (Zeiss). 3D-reconstruction of z stack images and inspection of neuronal morphology in virtual reality (VR) were conducted with SyGlass software (IstoVisio) using Oculus Rift S VR headsets and controllers (Oculus). SpineJ software (Levet et al., 2020) was used to analyze the basic spine morphology features from maximum projection images of dendrites. The overall tissue sizes were uniformly expanded due to the clearing process as previously reported (Park et al., 2019; Kim et al., 2015b) which reduced the spine density and increased the spine length compared to those of the original specimen.

RNA isolation and polymerase chain reaction (PCR) test—Five weeks after viral injection, mice were sacrificed and total RNA from mouse brain tissues was isolated using PureLink™ RNA Mini Kit (ThermoFisher Scientific/Invitrogen™) according to the manufacturer's instructions. Reverse transcription was performed with M-MLV reverse transcriptase (Invitrogen™) and random hexamers. PCR was performed with DreamTaq™ Hot Start Green PCR Master Mix (ThermoFisher Scientific) using T100 Thermal Cycler (Bio-Rad) equipment. The primers were 5′-GTCCAGCTACACAGCACAGA-3′ and 5′-GTTGCGGAGAACCTTCAGGA-3′ for Shank3 exon 4–5, 5′-CAAGTTCATCGCTGTGAAGG-3′ and 5′-TGTCGCATCTGCACTTCTTC-3′ for *Shank3* exon 11–12, and 5′-TCACCCACACTGTGCCCATCTACGA-3′ and 5′-CAGCGGAACCGCTCATTGCCAATGG-3′ for b-actin. The PCR conditions for *Shank3* mRNA were as follows: initial denaturation at 95°C for 3 min; 31 cycles of denaturation at 95°C for 20 s, annealing at 58°C for 20s, and elongation at 72°C for 20 s; final extension at 72°C for 5 min. The PCR for b-actin mRNA amplification was performed for 25 cycles under the same condition. The PCR products generated by each set of primers were subjected to agarose gel electrophoresis and band intensity was analyzed using ImageJ software.

Patch-clamp experiments—Eight weeks after viral injection, mice were sacrificed and brain slices were prepared using a modified protocol of acute brain slice methods for adult animals (Ting et al., 2014). Mice were anesthetized with isoflurane, and were perfused with N-methyl-D-Glutaminecation solution (NMDG-aCSF) bubbled with 95% O_2 and 5% CO_2 at room temperature (RT). The NMDG-aCSF solution contained the following (in mM): 92 NMDG, 2.5 KCl, 1.25 NaH_2PO_4, 30 $NaHCO_3$, 20 HEPES, 25 D-Glucose, 2 Thiourea, 5 Na-ascorbate, 3 Na-pyruvate, 0.5 $CaCl_2$, 10 $MgSO_4.7H_2O$, pH adjusted to 7.4 with HCl and osmolarity set to ~315 mOsm. After perfusion, brains were gently removed to oxygenated NMDG-aCSF in RT for 1 min, coronal slices were cut with the thickness of 400 μm using Leica VT1200S vibratome. The slices were then placed in oxygenated NMDG-aCSF at 30–32°C for less than 12 min. Then, the slices were recovered in oxygenated HEPES-aCSF ([in mM] 92 NaCl, 2.5 KCl, 1.25 NaH_2PO_4, 30 $NaHCO_3$, 20 HEPES, 25 D-Glucose, 2 Thiourea, 5 Na-ascorbate, 3 Na-pyruvate, 2 $CaCl_2$, 2 $MgSO_4.7H_2O$, pH adjusted to 7.4 with HCl and osmolarity set to ~315 mOsm) at room temperature for 1 h. During recording, slices were kept in oxygenated external bath solution (Recording aCSF: [in mM] 119 NaCl, 2.5

KCl, 1.25 NaH_2PO_4, 24 $NaHCO_3$, 12.5 D-Glucose, 2 $CaCl_2$, 2 $MgSO_4.7H_2O$, pH adjusted to 7.4 with HCl and osmolarity set to ~310 mOsm) at 28–30°C and a flow rate of 2–3 mL/min. Circuit neurons were identified with tdTomato signals, and neurons at the prelimbic (PL) region were recorded. Recording pipettes (3–5.5MΩ) contained varying internal solution depending on the purpose of the experiments. Recordings were performed with CV-7B headstage (Axon instruments) connected to Multiclamp 700B amplifier (Molecular Devices). Signals were filtered at 10 kHz and digitized at 20 kHz with the Digidata 1440A digitizer (Molecular Devices). The mEPSC, mIPSC, and action potentials were detected using pCLAMP10 software.

Voltage-clamp—During voltage-clamp experiments, cells were held at −70mV after making whole-cell contact and breaching membrane.

For mEPSCs (miniature excitatory postsynaptic current), 1 μM tetrodotoxin and 50 μM picrotoxin were mixed into bath solution. Internal pipette solution contained following: (in mM) 120 Cs methane sulfonate, 5 NaCl, 10 Tetraethyl ammonium chloride, 10 HEPES, 4 Lidocaine N-Ethyl Bromide, 1.1 EGTA, 4 Mg ATP, 0.3 Na GTP, pH adjusted to 7.2 with CsOH and osmolarity set to ~290 mOsm. Brain slices from WT (n = 3) and ctMUT (n = 3) were used. Total 12 WT neurons and 10 ctMUT neurons were recorded.

For mIPSC (miniature inhibitory postsynaptic current), 1 μM tetrodotoxin and 20 μM D-AP5 (D-2-amino-5-phosphonopentanoic acid) and 50 μM DNQX (6, 7-dinitroquinoxaline-2,3-dione) were mixed into bath solution. Internal pipette solution contained following: (in mM) 110 CsCl, 30 K-Gluconate, 0.1 $CaCl_2$, 10 HEPES, 1.1 EGTA, 4 MgATP, 0.3 MgGTP, pH adjusted to 7.2 with CsOH and osmolarity set to ~290 mOsm. Brain slices from WT (n = 6) and ctMUT (n = 4) were used. Total 20 WT neurons and 20 ctMUT neurons were recorded.

Current-clamp—During current-clamp experiments, after making whole-cell contact and breaching membrane, 8 steps of fixed current injections were given (−300pA–400pA, 100pA/step, current injection duration: 1s, inter-injection interval: 9s). Resting membrane potentials were also recorded during the experiments. No drug was mixed into the external bath solution. Internal pipette solution contained following: (in mM) 150 K-Gluconate, 2 $MgCl_2$, 1.1 EGTA, 10 HEPES, 3 Na-ATP, 0.2 Na-GTP, pH adjusted to 7.2 with KOH and osmolarity set to ~290 mOsm. Brain slices from WT (n = 3) and ctMUT (n = 3) were used. Total 15 WT neurons and 12 ctMUT neurons were recorded.

Behavioral tests—All the behavioral tests were conducted at the age of 3–5 months.

Open field test: Mice were placed into a square (37 × 37 × 36 cm) arena for 9 min under 180 lx illumination. EthoVision XT (Noldus) software tracked positions of the mouse 25 frames per second, and measured its traveled distance and mean velocity as well as the duration of time spent in the center (23 × 23 cm) and the margin of the arena. Using recorded videos, grooming behaviors were manually scored by the experimenters.

Round social arena (RSA) test: To precisely analyze the comprehensive social behaviors of mice, we developed a social testing paradigm, Round Social Arena (RSA). The uniform-environment-arena minimizes other attracting factors and spatial preferences (corners, sides, visual cues, shades, etc.) that occur in the classical 3-chamber test, enabling test mice to focus on social stimuli, leading to the enhanced probability of stable social interactions (data not shown). Moreover, RSA's uniform environment allows simpler behavioral patterns that are favorable for *in vivo* Ca^{2+} imaging to collect comparatively refined behavior-related neural data. The apparatus for RSA is a round-shaped arena (inner diameter: 49 cm, height: 45 cm) with one 3d-printed transparent bar cage (diameter: 8cm, height: 10.5 cm) at the center of the arena. The inner cage was topped with a cone-shaped 3d-printed roof to prevent the test mouse from climbing up. Inside the cone roof, a wide-angle (180°) fish-eye lens camera was installed to provide a close-up view of animals' social interactions. Above the arena, a camera at the ceiling was used to track animal's positions and speed. The experimental procedure consisted of two consecutive 10 min stages with 5 min interval: empty, and social (Figure 3C). The arena was illuminated at 35 lx during both stages. During the empty stage, the test mouse was allowed to freely explore the arena but the inner cage was empty. After 10 min, the mouse was removed to its home cage and a female juvenile (p30 ~ p50) C3H/HeJ mouse was introduced inside the inner cage. During the social stage, the test mouse was placed into the arena again and its social interaction with the social stimulus mouse was monitored. A virtual circular zone (3 cm around the inner cage) was designated as S-Zone and the subject animal's entry to this zone *via* its nose was measured by the EthoVision XT software (Noldus). Using video recordings from fish-eye lens camera, social behaviors such as sniffing and reciprocal sniffing were manually scored. Sniffing was defined as the test mouse actively exploring the cage with its nose directed toward the cage. Reciprocal sniffing was defined as both the test and social stimulus mice exhibiting sniffing behavior with their noses directed to each other. All test mice and social stimulus mice were habituated to the arena for 2 days (15 min/day) separately before the experiment. All test mice were isolated in single-housing cages for 1 week before the experiment.

Light-dark box test: The light-dark box test arena consists of two adjoining chambers: a lighted chamber (600 lx), and a dark chamber (under 5 lx) which are divided by a manually removable door. Before testing, the mouse was placed in the dark chamber for 1 min. The testing was started by opening the door, and the mouse was given full access to the entire apparatus for 5 min. The time spent in each chamber, mean duration of entry to each chamber was analyzed by EthoVision XT (Noldus) software.

Marble-burying test: The marble-burying test was conducted in a wide cage ($48 \times 27 \times 20$ cm) with beddings. Twenty glass toy marbles (blue, 1.5cm diameter, 5.2g in weight) were gently placed on the surface of the beddings in 5 rows of 4 marbles. After a test mouse was placed into a corner of the cage, a filter-top cover was placed on the cage and the test mouse was allowed full access for 30 min. After moving the test mouse to its home cage, experimenters scored the number of buried marbles. A marble was scored as buried if two-thirds of its surface area was covered by bedding.

Rotarod: The rotarod test was conducted using Rotamex (Columbus Instruments). The speed of the rotating rod initiated at 4 RPM, and increased in steps of 4 RPM every 30 s until it reached 48 RPM. The latency to fall and the speed at which the animal fell were measured. All 6 trials were conducted at intervals of 10 min.

Non-social olfactory investigation: To test sniffing behavior and underlying neural response to non-social objects, two tactile stimuli (velcro loop, sponge) were placed in the opposite walls of the round arena. Mice were allowed to explore and investigate the tactile stimuli for 10 min.

Cued fear conditioning and test: Cued fear conditioning was conducted using a custom-built fear conditioning chamber (context A; 20 cm × 25 cm × 18 cm) with a loudspeaker and metal grid floor for electric shock. A custom-written Arduino code controlled the delivery of conditional stimulus (CS; tone, 2 kHz, 65dB, 20s) and unconditional stimulus (US; electric footshock, 1.2mA, 1s). Infrared LED indicated the presentation of CS and US (Video S2). Animals were habituated to the chamber (5 min/day) for 3 days prior to the conditioning. On conditioning day, animals were habituated to the chamber again for 5 min and conditioning protocol conceded. Fear conditioning consisted of 5 trials of CS + US presentation (20s CS co-terminating with 1s US presentation). A day after conditioning, a tone test was conducted in context B (transparent plastic cylinder; 15cm diameter, 25 cm height). After 2 min of baseline observation, 3 trials of CS presentation were given. During fear conditioning and test session, animals' freezing behaviors were scored with EthoVision XT (Noldus) software, and Ca^{2+} activity was simultaneously recorded. Neurons responsive to the US or CS were identified using two criteria: 1) averaged normalized Ca^{2+} transient during event 2.0 standard deviations higher above the mean, and 2) significantly higher values above the baseline period confirmed by Wilcoxon rank-sum test ($p < 0.05$). The number of event-responsive neurons were as follow: US-responsive neurons (WT: n = 28; ctMUT: n = 71), and CS-responsive neurons (WT: n = 11; ctMUT: n = 31).

Ca^{2+} imaging with a head-mounted fluorescent microscope

Surgery: Four-weeks after viral injections of male WT (n = 8) and *Shank3*$^{f/f}$ (e4-9) (ctMUT; n = 10) mice, gradient index (GRIN) lenses (Inscopix ProView™ lens; 1mm diameter/4mm length) were unilaterally implanted in the PL region of PFC (AP: +2.5 mm, ML ±0.5 mm, DV: –0.5 mm). Once in place, the lens was secured to the skull using a C&B-Metabond (Parkell) cementing over two anchoring screws on the skull. Two weeks after the GRIN lens implantation, the baseplate (Inscopix) was mounted onto the GRIN lens under visual guidance *via* a miniature microscope (Inscopix) to determine the best field of view (FOV).

Behavior: One week before RSA, mice were isolated in single-housing cages. Behavioral experiments with GCaMP7f imaging were conducted in the following order: open field and RSA. A day before the open field test, testing mice were connected with a dummy microscope and habituated to its weight for 10 min in their home cages. Before RSA, testing mice were connected to a dummy microscope and habituated in the arena for 2 days (10 min/day). During RSA, the Ca^{2+} signals were recorded by miniature microscope and nVista

DAQ system (Inscopix) with 20 fps in synchronization with behavioral data collected by EthoVision XT and Fish-eye lens camera.

Image processing: All Ca^{2+} imaging movies obtained by nVista system were initially preprocessed using the Inscopix Data Processing Software (IDPS; Inscopix). The movies were down-sampled spatially ($\times 4$) and temporally ($\times 2$: to 10 fps) to reduce computational load. Then spatial bandpass filtering was conducted using global mean subtraction, and motion correction was applied. We then implemented the constrained non-negative matrix factorization (CNMFe) algorithm written in MATLAB (Mathworks) scripts for simultaneous denoising, deconvolving, and demixing of Ca^{2+} signals as well as automatic cell identification (Pnevmatikakis et al., 2016). The cells identified by CNMFe were re-analyzed in IDPS and manually revised by the experimenter whether to be accepted as a neuron or to be rejected. Among the total 1,787 neurons acquired from all 18 animals, 675 neurons were found in WT animals (n = 8) and 1,112 neurons were found in ctMUT animals (n = 10).

Single neuron analyses: For each neuron, Ca^{2+} transient events were calculated using a threshold of 2.0 standard deviation above the mean. The mean amplitude and amplitude-variance of these transient events were measured. We then used the procedure described in previous studies (Liang et al., 2018; Carrillo-Reid et al., 2015; Hamm et al., 2017) to identify behaviorally tuned neurons. In brief, (1) F/F trace of each neuron was vectorized in f-dimensional space (f = number of frames) as C_n. (2) We calculated the similarity between each neuron's Ca^{2+} trace (F/F) vector C_n and the behavior vector B (Figure 5B). Similarity was defined as the modified cosine similarity between two vectors which is a value between 0 and 1:

$$\text{Similarity index}^{B, C_n} = 2B \cdot C_n / \left(\mid B \mid^2 + \mid C_n \mid^2 \right).$$

A value of 1 indicates that two vectors are identical while 0 means that they are completely opposite. (3) To verify the significance of behavior-neuron similarity, we used a bootstrapping procedure. We randomly shuffled behavior epochs and calculated the similarity between the shuffled behavior vector and the neuron's Ca^{2+} trace vector C_n. By repeating this process 5,000 times, a null similarity distribution histogram was generated which represents the similarity distribution predicted by chance for a given neuron (Figure S5A). (3) A neuron was determined as an "ON neuron" only if the actual similarity value was greater than the 99.17th quantile of the null similarity distribution. A neuron was determined as an "OFF neuron" only if the actual similarity value was lower than the 0.83th quantile of the null similarity distribution.

Neural ensemble decoding analyses using machine learning classifier: We hypothesized that a specific social behavior could be predicted by the patterns of neural circuit activities. To address this hypothesis, we conducted neural decoding analyses (Figure S10A). For each mouse, the population of simultaneously recorded neurons during an experiment was considered an ensemble. To determine an ensemble, 3 different criteria were used: (1) All neurons, (2) social-ONOFF neurons, and (3) True other neurons. The 'Social ONOFF

neurons' included any neurons that are tuned as 'ON' or 'OFF' to social behaviors (sniffing, S-Zone entry, and reciprocal sniffing). The 'True other' neurons were any neurons that are not included in the 'social-ONOFF neurons.

Using scikit-learn in Python, a machine learning classifier (fine decision tree; split-criteria: gini, maximum depth: none, minimum samples for split: 2, minimum samples for leaf: 1) was trained to predict four classes of exclusive behaviors [a: arena (outside of S-Zone), b: S-Zone (no sniffing), c: sniffing (no reciprocal sniffing), d: reciprocal sniffing; Figure S10B] from an ensemble. In detail, (1) each frame (10 fps) containing an ensemble of Ca^{2+} traces with a label for the concurrent behavior was defined as a dataset. Datasets for each behavior class were down-sampled to fit the minimum class size, in order to equalize the sizes of all four classes and to avoid any biased learning during the training procedure. (2) Then 10-fold cross-validation process was applied. Datasets were randomly assigned to 10 subgroups, and in each validation process, 9 subgroups were used for training the classifier and the remaining 1 subgroup was used to test the accuracy of the trained classifier. This process was repeated 10 times until all 10-fold cross-validation was complete. The overall accuracy of the classifier was obtained from all test results, and the accuracy for each class was displayed in a confusion matrix (Figures S10C, S10D, S10H, S10I, S10J, S10K). To confirm whether these decoding accuracies are significant, control datasets were generated by shuffling the labels of the original datasets. The same 10-fold cross-validation process was applied to these control datasets. The decoding accuracies for the control datasets were around the chance level (25%), and the statistical tests (independent t test) were conducted to verify the significance of differences between the decoding accuracies of the actual datasets and the control datasets (Figures S10C and S10D - right panels).

The analysis for the ensembles from the WT neurons revealed high prediction accuracies for all four behaviors (78.63–95.95%) (Figure S10C), confirming that the PFC-BLA circuit neurons encode social behaviors. To our surprise, the ensembles from the ctMUT neurons also predicted the social behaviors with similar accuracies (71.07–96.10%) (Figure S10D), suggesting that despite the reduced temporal correlation, the neural ensemble patterns of ctMUT neurons are likely to be sufficient for the machine learning algorithms to predict social behaviors.

We next measured the contribution rates of each class of neurons for the behavior prediction using a 'feature importance analysis'(Casalicchio et al., 2018), using the scikit-learn function. The mean feature importance of each class of neurons (social-ON, OFF, and True Other) was compared within an ensemble. As feature importance was relative to the total number of neurons in an ensemble (sum of feature importance = 1), the mean feature importance values displayed different ranges and thus could not be pooled across multiple ensembles. However, it was possible to compare the summed feature importance values for each class of neurons between different ensembles. The analysis showed that social-ON neurons have the highest mean feature importance in contributing to the prediction accuracy (Figures S10E and S10F).

It is important to note that due to comprising a majority of the population in the circuit (74–84%), True Other neurons showed the highest summed feature importance values over

the Social-ON and OFF neurons (Figures S10E-S10G). To confirm the participation of True Other neurons in the social behaviors, we conducted decoding analysis again with ensembles only from social-ON and OFF neurons or only from True Other neurons (Figures S10H-S10K). Data revealed that the ensembles of True Other neurons from both WT and ctMUT also predicted each social behavior at a similar accuracy level of the social-ON and OFF ensembles (Figures S10J and S10K). These results suggest that the True Other neurons that were assigned as socially-untuned neurons may also encode information for social behaviors *via* an unknown encryption rule that may be different from the simple correlation suggested by the similarity comparison. Also, all four behaviors were successfully predicted by the ensembles from *Shank3* ctMUT mice (Figures S10D, S10I and S10K).

Neural ensemble network graph theory analyses: Since the machine learning analysis provided evidence that social ON, OFF, and True other neurons were all involved in social behaviors, we next sought to find out how each type of neuron is associated within the PFC-BLA intra-circuit functional network, and how they were affected by the *Shank3* ctMUT. In brief, we visualized the functional network dynamics between the activity of the circuit neurons. For this analysis, we implemented a method modified from the procedure described in a previous study (Jimenez et al., 2020) and graph theory analysis metrics used in the study of social media (Golbeck, 2013). Using the NetworkX python package and custom python scripts, the higher-order structure of the neural correlations was visualized and quantified (Figure S10O). Each circuit neuron was presented as a node (red: social ON, blue: social OFF, gray: True other) and the significant similarity between a pair of neurons was drawn as an edge (orange line) (Jimenez et al., 2020) (Figures S10N and S10O). To calculate the similarity of every pair of simultaneously recorded neurons, the similarity between their Ca^{2+} traces was calculated (Figure S10L) using the procedure described in previous studies (Hamm et al., 2017; Cossart et al., 2003). In brief, (1) we calculated the modified cosine similarity between two neurons' Ca^{2+} trace vectors C_a and C_b:

$$\text{Similarity index}^{C_a, C_b} = 2C_a \cdot C_b / \left(|C_a|^2 + |C_b|^2 \right).$$

The value of this index ranged from 0 to 1 (1 indicating two vectors are identical and 0 indicating that they are opposite). (2) To confirm the significance of the similarity between cell pairs, a bootstrapping procedure was used. Individual neurons' Ca^{2+} trace vectors were shifted by random amounts in time separately for each cell, generating a surrogate dataset. Then mean pairwise similarity values were calculated for all surrogate cell pairs. This step was repeated 10,000 times, creating a null similarity distribution that represents the distribution of similarities predicted at the chance level for every pair of neurons (Figure S10M). The actual cell pair similarities that exceed the 99.17th quantile of null similarity distribution were considered significant.

Only mice with more than 100 neurons per FOV were included in the analysis (WT; n = 3, ctMUT; n = 4), due to the sampling limitation of correlated cell pairs in a network with sparse FOV. In both empty and social stages, all types of neurons formed a complex network within an ensemble (Figure S10P) and the percentage of significant edges over all possible connections between neurons increased from empty to social stage, but with no significant

difference between groups (Figure S10O). Thus, in order to quantify the differences in network structures between groups, we measured the network complexity using two graph theory metrics: the degree centrality and the eigenvector centrality (Golbeck, 2013). The degree centrality of a node is the number of its edges normalized by the maximum possible edges (Figure S10Q).

$$\text{Degree centrality of a node N} = (\text{\# of edges connected to N}) \, / \, (n-1)$$

n = number of nodes in the graph.

The degree centrality of a node was calculated by obtaining the number of edges connected to the node and dividing it by the maximum possible degree in the graph (n-1; n = number of all nodes).

$$\text{Eigenvector centrality of a node N} = x_N, \; (Ax = \lambda x; \; A: \text{Adjacency matrix}; \; \lambda: \text{Eigenvalue})$$

The eigenvector centrality is a measure of a node's influence in the network. It measures the node's importance in consideration of the importance of its neighbors. It was calculated by performing a matrix calculation using the adjacency matrix of edges to determine the principal eigenvector. Neighboring nodes with higher degree centrality increased the starting node's eigenvector centrality, well representing how its influence propagates through the network.

Regardless of the groups, all types of neurons contributing to the network of social behaviors showed a significant increase in degree centrality as the test mouse is transferred from an empty stage to social stage, indicating a social behavior-induced dynamic formation of complex connections (Figures S10R-S10T). Interestingly, only the ctMUT True other neurons showed significantly higher degree centralities than those of WT in both stages (Figure S10T), suggesting an upregulated basal network complexity of True other neurons in *Shank3* ctMUT mice.

The eigenvector centrality of the ctMUT social-ON neurons was significantly enhanced by social interaction, whereas the WT social-ON neurons did not show a significant change (Figure S10V). Meanwhile, the social OFF and True other neurons of each group across the stages did not show any differences (Figures S10W and S10X), suggesting that the social behavior-specific ctMUT social-ON neurons' hyperactivity (Figures 6C and 6D) likely increased the influence over all neurons within the intra-circuit network. However, the decreased neural activity of ctMUT social-OFF neurons during social behaviors may not affect the network complexity.

Optogenetics

Optic fiber implant surgery: Two weeks after viral infection, control and experimental animals received optical probe implant surgery. In brief, flat-cut fiber-optic probes (400μm fiber core diameter, 1.25mm OD ferrule, 0.5NA; RWD Life Science Inc.) were bilaterally lowered to the PFC (AP: +2.5 mm, ML: +0.8 mm, DV: −0.5 mm from brain surface) and

secured by applying a C&B-Metabond (Parkell) cement covering two anchoring screws on the skull.

Optical stimulation configuration (optogenetic activation): A single blue LED light (473nm) generated by Dual-Channel-Optogenetics LED (Prizmatix) was split with a 1 × 2 optical commutator (Doric) to deliver ~5mW optical power to each hemisphere. Optical stimulation was controlled by a train of TTL pulses (pulse width: 5ms, pulse frequency: 5 Hz) generated by Prizmatix pulse generator which was controlled by TTL input from EthoVision XT (Noldus) software that determined the criteria for initiation and termination of stimulation.

Behavior (optogenetic activation): One week after optical implant surgery, animals were isolated to single-housing cages. After another week, animals were connected to bilaterally split optic fibers and were habituated to RSA for 2 days (10 min/day) without actual optical stimulation. Testing consisted of four 10-min sessions (empty, baseline-social, 5 Hz-social, 5-Hz empty) conducted on different days. During the empty stage, the inner cage was empty and no optical stimulation was given. During the baseline-social stage, a female C3H/HeJ (p30-p50) mouse was placed inside the inner cage, but no optical stimulation was given in order to monitor the test mice's baseline sociability. In 5 Hz-social stage, a new female C3H/HeJ mouse was placed inside the inner cage and an optical stimulation was triggered when the test mouse's nose entered the S-Zone (3 cm around the inner cage) and terminated as the mouse exited the zone. One week after the 5 Hz-social stage, an additional 5 Hz-empty stage was conducted. Without any social stimulus, optical stimulation was given when the test mouse entered the S-Zone. Throughout all stages, social behaviors such as sniffing, S-Zone entry, and reciprocal sniffing were measured.

Optical stimulation configuration (optogenetic inhibition): Configurations were the same as the optogenetic activation experiment except for LED light properties (520 nm, constant during stimulation).

Behavior (optogenetic activation): Behavioral testing protocol was the same as the optogenetic activation experiment. However, only three sessions (empty, baseline-social, conditional inhibition) were conducted.

Human neuroimaging

Participants: We analyzed human rs-fMRI which represents an intrinsic, standard state of brain architecture (Cole et al., 2014; Smith et al., 2009). The rs-fMRI were obtained from the ABIDE dataset (Di Martino et al., 2014), which is available on the Mind Research Network's collaborative informatics and neuroimaging suite (COINS) data exchange (Landis et al., 2016). The initial dataset consisted of 406 ASD individuals and 432 control (typical development) individuals. We excluded individuals that are (1) without full-coverage of both T1 anatomical and EPI images, (2) with less than 100 EPI volumes to obtain reliable connectivity metrics, (3) with severe motions for EPI images (mean framewise displacement, FD > 0.25 mm) because motion artifacts may alter connectivity metrics of rs-fMRI (Power et al., 2012, 2014) and (4) with noise-contaminated

T1 anatomical images. In this stage, 263 ASD and 325 control individuals remained. The age criteria were set based on quartiles of age distribution of the initial dataset (Riddle et al., 2017). Therefore, individuals whose ages at 6–11.56 during scan were selected for further analysis. This resulted in 72 ASD (M = 9.77 years, SD = 1.27, female = 15.28%) and 72 control (M = 9.59 years, SD = 1.22, female = 29.17%). There was no group difference in age (t(142) = −0.892, p = 0.374).

fMRI data preprocessing: We preprocessed the rs-fMRI data using FMRIB Software Library (FSL) (Jenkinson et al., 2012). The preprocessing included 0.001–0.08 Hz band-pass filtering, first 10 volumes cut-off, motion correction, slice-timing correction, grand-mean intensity normalization to the whole 4D data, regressing out CSF/WM nuisance signals, ICA denoising on motion and physiological noise using ICA-AROMA (Pruim et al., 2015) and MELODIC (Beckmann and Smith, 2004), and nonlinear transformation spatial normalization to 2-mm MNI EPI template using Advanced Normalization Tool library (ANTs) (Avants et al., 2011). We did not adopt Gaussian smoothing as the amygdala is a relatively small region in the brain and thus the smoothing may cause the mixed-signal with neighboring non-amygdala voxels. For the WM/CSE nuisance regressors, we extracted signals within WM/CSF anatomical masks at 90% probability segmented by the FAST (Zhang et al., 2001).

mPFC-amygdala functional connectivity: To test our hypothesis, we extracted the mean time-series of mPFC using predefined mPFC mask (Figure 4A; the number of voxel = 5,257) from 90 fROIs dataset (Shirer et al., 2012). The amygdala mask was defined by combining left and right amygdala masks in the automated anatomical labeling (AAL) 2 atlas (Rolls et al., 2015). In addition, primary motor area time-series was also extracted using bilateralized postcentral masks in AAL2 atlas to serve as a control ROI against mPFC-amygdala connectivity. Since there were no explicit motor activities in resting-state MRI acquisition, the primary motor area has been suggested to serve as a control ROI (Antonenko et al., 2017). Using the control ROI, we could estimate whether the mPFC-amygdala connection is one of the ASD-specific connections or not. From these time-series, the static functional connectivity (static-FC) values were calculated by pairwise Pearson's correlation on whole-length signals with fisher's z-transform (Figure 4B; dotted square). As studies have suggested that rs-fMRI has a dynamic nature (Li et al., 2020) and static-FC can be distorted by a slow dynamic fluctuation of the time-series, we also examined connectivity difference between the groups with dynamic functional connectivity (dynamic-FC). In the dynamic-FC analysis, we adopted a sliding-window approach using the Dynamic Correlation Toolbox with 40 TR window size and 1 TR shift. We also used different size of sliding-window as 30 TR and 50 TR, the results were consistent (See Tables S1A and S1B). The mean of dynamic-FC was calculated across multiple z-transformed correlation coefficients of sliding-windows (Figure 4B; solid square). We also calculated the moment-to-moment variability of dynamic-FC using the MSSD (von Neumann et al., 1941). Specifically, the MSSD was calculated by subtracting the dynamic-FC value at t time point from t+1 time point and then squaring the result. The squared values were then averaged. High MSSD means there is more moment-by-moment connectivity variability between ROIs.

Support vector machine classification based on dynamic-FC values—We also assumed that dynamic-FC values of mPFC-amygdala themselves could be used to classify ASD and control given that the dynamic-FC values array contain information about both mean and variability of dynamic-FC. We used the same time-series extracted from mPFC and amygdala ROIs. However, in this analysis, the time-series were trimmed to first 110 volumes to unify the size of multi-feature dimension. The size of 110 volumes was the minimum volume length of the remained individual EPI data. From extracted time-series, dynamic-FC values were calculated with the same parameters (40TR) and then z-transformed. The calculated dynamic-FC values were put to a linear support vector machine (SVM). We used the MVPA-Light toolbox (Treder, 2020) to classify the dynamic-FC values between ASD and control with a 5-fold cross-validation scheme and 15 repetitions to get reliable classification accuracies. The area under curve (AUC) value was calculated as classification accuracy, and the significance of AUC was determined as the value higher than the 95th quantile of a null decoding accuracy distribution obtained from 5,000 label-shuffled permutations.

QUANTIFICATION AND STATISTICAL ANAYSIS

All bar graphs are presented as mean ± SEM and all box and whiskers graphs display the median, the upper and lower quartiles, and minimum and maximum values. Statistics were analyzed using GraphPad Prism 9.0 (GraphPad), SPSS 25 (IBM), and MATLAB (Mathworks) software. Independent t test was used to analyze the genotypical differences of mean mEPSC amplitude and frequency as well as mean mIPSC amplitude and frequency, and the resting membrane potentials. To analyze cumulative probability distribution of mEPSC and mISPC amplitudes, or their inter-event-intervals, Kolmogorov-Smirnov test was used. two-way ANOVA with repeated measures was used for the analysis of differences between two groups (WT, ctMUT) in neuronal excitability and social behaviors. Two-stage linear step-up procedure of Benjamini, Kreger and Yekutieli comparisons were used as post-hoc corrections. For analyses of Ca^{2+} trace amplitude, amplitude variance, Ca^{2+} trace-behavior similarity values which fail to pass normal distribution assumption (Shapiro-Wilk test, $p < 0.05$), Mann-Whitney U tests were conducted. Group comparisons that met the normal distribution assumption (Shapiro-Wilk test, $p > 0.05$) and do not require repeated measures were analyzed with independent t-tests. Similarly, in metrics derived from human neuroimaging data including static-FC, mean of dynamic-FC and MSSD, independent t-tests were used to compare the ASD and the control. Spearman's rank correlation coefficient was used to assess the non-linear, but monotonic relationships between Ca^{2+} amplitude, amplitude variance, and Ca^{2+} trace-behavior similarity indices. Pearson's correlation coefficient was used to analyze the correlative relationship between the duration of social behavior and the Ca^{2+} amplitude. All the detailed statistical results are listed in Table S1E.

Supplementary Material

Refer to Web version on PubMed Central for supplementary material.

ACKNOWLEDGMENTS

REFERENCES

Adolphs R (2003). Cognitive neuroscience of human social behaviour. Nat. Rev. Neurosci 4, 165–178. 10.1038/nrn1056. [PubMed: 12612630]

Amodio DM, and Frith CD (2006). Meeting of minds: the medial frontal cortex and social cognition. Nat. Rev. Neurosci 7, 268–277. 10.1038/nrn1884. [PubMed: 16552413]

Antonenko D, Schubert F, Bohm F, Ittermann B, Aydin S, Hayek D, Grittner U, and Flöel A (2017). tDCS-induced modulation of GABA levels and resting-state functional connectivity in older adults. J. Neurosci 37, 4065–4073. 10.1523/jneurosci.0079-17.2017. [PubMed: 28314813]

Avants BB, Tustison NJ, Song G, Cook PA, Klein A, and Gee JC (2011). A reproducible evaluation of ANTs similarity metric performance in brain image registration. Neuroimage 54, 2033–2044. 10.1016/j.neuroimage.2010.09.025. [PubMed: 20851191]

Barker GRI, Banks PJ, Scott H, Ralph GS, Mitrophanous KA, Wong L-F, Bashir ZI, Uney JB, and Warburton EC (2017). Separate elements of episodic memory subserved by distinct hippocampal–prefrontal connections. Nat. Neurosci 20, 242–250. 10.1038/nn.4472. [PubMed: 28067902]

Beckmann CF, and Smith SM (2004). Probabilistic independent component analysis for functional magnetic resonance imaging. IEEE Trans. Med. Imaging 23, 137–152. [PubMed: 14964560]

Berkel S, Eltokhi A, Frohlich H, Porras-Gonzalez D, Rafiullah R, Sprengel R, and Rappold GA (2018). Sex hormones regulate SHANK expression. Front. Mol. Neurosci 11, 337. 10.3389/fnmol.2018.00337. [PubMed: 30319350]

Bey AL, Wang X, Yan H, Kim N, Passman RL, Yang Y, Cao X, Towers AJ, Hulbert SW, Duffney LJ, et al. (2018). Brain region-specific disruption of Shank3 in mice reveals a dissociation for cortical and striatal circuits in autism-related behaviors. Transl. Psychiatry 8, 94. 10.1038/s41398-018-0142-6. [PubMed: 29700290]

Bicks LK, Koike H, Akbarian S, and Morishita H (2015). Prefrontal cortex and social cognition in mouse and man. Front. Psychol 6, 1805. 10.3389/fpsyg.2015.01805. [PubMed: 26635701]

Bossert JM, Stern AL, Theberge FR, Marchant NJ, Wang H-L, Morales M, and Shaham Y (2012). Role of projections from ventral medial prefrontal cortex to nucleus accumbens shell in context-induced reinstatement of heroin seeking. J. Neurosci 32, 4982–4991. 10.1523/jneurosci.0005-12.2012. [PubMed: 22492053]

Bozdagi O, Sakurai T, Papapetrou D, Wang X, Dickstein DL, Takahashi N, Kajiwara Y, Yang M, Katz AM, Scattoni ML, et al. (2010). Haploinsufficiency of the autism-associated Shank3 gene leads to deficits in synaptic function, social interaction, and social communication. Mol. Autism 1, 15. 10.1186/2040-2392-1-15. [PubMed: 21167025]

Carrillo-Reid L, Miller J-EK, Hamm JP, Jackson J, and Yuste R (2015). Endogenous sequential cortical activity evoked by visual stimuli. J. Neurosci 35, 8813–8828. 10.1523/jneurosci.5214-14.2015. [PubMed: 26063915]

Casalicchio G, Molnar C, and Bischl B (2018). Visualizing the feature importance for black box models. In Joint European Conference on Machine Learning and Knowledge Discovery in Databases (Springer), pp. 655–670.

Chen Q, Deister CA, Gao X, Guo B, Lynn-Jones T, Chen N, Wells MF, Liu R, Goard MJ, Dimidschstein J, et al. (2020). Dysfunction of cortical GABAergic neurons leads to sensory hyper-reactivity in a Shank3 mouse model of ASD. Nat. Neurosci 23, 520–532. 10.1038/s41593-020-0598-6. [PubMed: 32123378]

Cole MW, Bassett DS, Power JD, Braver TS, and Petersen SE (2014). Intrinsic and task-evoked network architectures of the human brain. Neuron 83, 238–251. 10.1016/j.neuron.2014.05.014. [PubMed: 24991964]

Cossart R, Aronov D, and Yuste R (2003). Attractor dynamics of network UP states in the neocortex. Nature 423, 283–288. 10.1038/nature01614. [PubMed: 12748641]

Dana H, Sun Y, Mohar B, Hulse BK, Kerlin AM, Hasseman JP, Tsegaye G, Tsang A, Wong A, Patel R, Macklin JJ, Chen Y, Konnerth A, Jayaraman V, Looger LL, Schreiter ER, Svoboda K, and Kim DS (2019). High-performance calcium sensors for imaging activity in neuronal populations and microcompartments. Nature methods 16, 649–657. 10.1038/s41592-019-0435-6. [PubMed: 31209382]

Di Martino A, Yan CG, Li Q, Denio E, Castellanos FX, Alaerts K, Anderson JS, Assaf M, Bookheimer SY, Dapretto M, et al. (2014). The autism brain imaging data exchange: towards a large-scale evaluation of the intrinsic brain architecture in autism. Mol. Psychiatry 19, 659–667. 10.1038/mp.2013.78. [PubMed: 23774715]

Durand CM, Betancur C, Boeckers TM, Bockmann J, Chaste P, Fauchereau F, Nygren G, Rastam M, Gillberg IC, Anckarsäter H, et al. (2007). Mutations in the gene encoding the synaptic scaffolding protein SHANK3 are associated with autism spectrum disorders. Nat. Genet 39, 25–27. 10.1038/ng1933. [PubMed: 17173049]

Felix-Ortiz AC, Burgos-Robles A, Bhagat ND, Leppla CA, and Tye KM (2016). Bidirectional modulation of anxiety-related and social behaviors by amygdala projections to the medial prefrontal cortex. Neuroscience 321, 197–209. 10.1016/j.neuroscience.2015.07.041. [PubMed: 26204817]

Fombonne E (2009). Epidemiology of pervasive developmental disorders. Pediatr. Res 65, 591–598. 10.1203/pdr.0b013e31819e7203.. [PubMed: 19218885]

Forbes CE, and Grafman J (2010). The role of the human prefrontal cortex in social cognition and moral judgment. Annu. Rev. Neurosci 33, 299–324. 10.1146/annurev-neuro-060909-153230. [PubMed: 20350167]

Franklin TB, Silva BA, Perova Z, Marrone L, Masferrer ME, Zhan Y, Kaplan A, Greetham L, Verrechia V, Halman A, et al. (2017). Prefrontal cortical control of a brainstem social behavior circuit. Nat. Neurosci 20, 260–270. 10.1038/nn.4470. [PubMed: 28067904]

Fried I, Macdonald KA, and Wilson CL (1997). Single neuron activity in human hippocampus and amygdala during recognition of faces and objects. Neuron 18, 753–765. 10.1016/s0896-6273(00)80315-3. [PubMed: 9182800]

Frost NA, Haggart A, and Sohal VS (2021). Dynamic patterns of correlated activity in the prefrontal cortex encode information about social behavior. PLoS Biol. 19, e3001235. 10.1371/journal.pbio.3001235. [PubMed: 33939689]

Gilbert SJ, Bird G, Brindley R, Frith CD, and Burgess PW (2008). Atypical recruitment of medial prefrontal cortex in autism spectrum disorders: an fMRI study of two executive function tasks. Neuropsychologia 46, 2281–2291. 10.1016/j.neuropsychologia.2008.03.025. [PubMed: 18485420]

Golbeck J (2013). Chapter 3-network structure and measures. In Analyzing the Social Web (Morgan Kaufmann), pp. 25–44.

Grossmann T (2013). The role of medial prefrontal cortex in early social cognition. Front. Hum. Neurosci 7, 340. 10.3389/fnhum.2013.00340. [PubMed: 23847509]

Guo B, Chen J, Chen Q, Ren K, Feng D, Mao H, Yao H, Yang J, Liu H, Liu Y, et al. (2019). Anterior cingulate cortex dysfunction underlies social deficits in Shank3 mutant mice. Nat. Neurosci 22, 1223–1234. 10.1038/s41593-019-0445-9. [PubMed: 31332372]

Hamm JP, Peterka DS, Gogos JA, and Yuste R (2017). Altered cortical ensembles in mouse models of schizophrenia. Neuron 94, 153–167.e8. 10.1016/j.neuron.2017.03.019. [PubMed: 28384469]

Harlalka V, Bapi RS, Vinod PK, and Roy D (2019). Atypical flexibility in dynamic functional connectivity quantifies the severity in autism spectrum disorder. Front. Hum. Neurosci 13, 6. 10.3389/fnhum.2019.00006. [PubMed: 30774589]

Hoehl S, Reid VM, Parise E, Handl A, Palumbo L, and Striano T (2009). Looking at eye gaze processing and its neural correlates in infancy–implications for social development and

autism spectrum disorder. Child Dev. 80, 968–985. 10.1111/j.1467-8624.2009.01311.x. [PubMed: 19630888]

Huang W-C, Chen Y, and Page DT (2016). Hyperconnectivity of prefrontal cortex to amygdala projections in a mouse model of macrocephaly/autism syndrome. Nat. Commun 7, 13421. 10.1038/ncomms13421. [PubMed: 27845329]

Huang W-C, Zucca A, Levy J, and Page DT (2020). Social behavior is modulated by valence-encoding mPFC-amygdala sub-circuitry. Cell Rep. 32, 107899. 10.1016/j.celrep.2020.107899. [PubMed: 32668253]

Hultman R, Mague SD, Li Q, Katz BM, Michel N, Lin L, Wang J, David LK, Blount C, Chandy R, et al. (2016). Dysregulation of prefrontal cortex-mediated slow-evolving limbic dynamics drives stress-induced emotional pathology. Neuron 91, 439–452. 10.1016/j.neuron.2016.05.038. [PubMed: 27346529]

Jaramillo TC, Speed HE, Xuan Z, Reimers JM, Liu S, and Powell CM (2016). Altered striatal synaptic function and abnormal behaviour in Shank3 exon4-9 deletion mouse model of autism. Autism Res. 9, 350–375. 10.1002/aur.1529. [PubMed: 26559786]

Jenkinson M, Beckmann CF, Behrens TE, Woolrich MW, and Smith SM (2012). FSL. Neuroimage 62, 782–790. 10.1016/j.neuroimage.2011.09.015. [PubMed: 21979382]

Jeon SJ, Gonzales EL, Mabunga DFN, Valencia ST, Kim DG, Kim Y, Adil KJL, Shin D, Park D, and Shin CY (2018). Sex-specific behavioral features of rodent models of autism spectrum disorder. Exp. Neurobiol 27, 321–343. 10.5607/en.2018.27.5.321. [PubMed: 30429643]

Jiang Y-H, and Ehlers MD (2013). Modeling autism by SHANK gene mutations in mice. Neuron 78, 8–27. 10.1016/j.neuron.2013.03.016. [PubMed: 23583105]

Jimenez JC, Berry JE, Lim SC, Ong SK, Kheirbek MA, and Hen R (2020). Contextual fear memory retrieval by correlated ensembles of ventral CA1 neurons. Nat. Commun 11, 3492. 10.1038/s41467-020-17270-w. [PubMed: 32661319]

Kennedy DP, and Adolphs R (2012). The social brain in psychiatric and neurological disorders. Trends Cogn. Sci 16, 559–572. 10.1016/j.tics.2012.09.006. [PubMed: 23047070]

Kim IH, Racz B, Wang H, Burianek L, Weinberg R, Yasuda R, Wetsel WC, and Soderling SH (2013). Disruption of Arp2/3 results in asymmetric structural plasticity of dendritic spines and progressive synaptic and behavioral abnormalities. J. Neurosci 33, 6081–6092. 10.1523/jneurosci.0035-13.2013. [PubMed: 23554489]

Kim IH, Rossi MA, Aryal DK, Racz B, Kim N, Uezu A, Wang F, Wetsel WC, Weinberg RJ, Yin H, and Soderling SH (2015a). Spine pruning drives antipsychotic-sensitive locomotion via circuit control of striatal dopamine. Nat. Neurosci 18, 883–891. 10.1038/nn.4015. [PubMed: 25938885]

Kim S-Y, Cho JH, Murray E, Bakh N, Choi H, Ohn K, Ruelas L, Hubbert A, Mccue M, Vassallo SL, et al. (2015b). Stochastic electrotransport selectively enhances the transport of highly electromobile molecules. Proc. Natl. Acad. Sci. U S A 112, E6274–E6283. 10.1073/pnas.1510133112. [PubMed: 26578787]

Kim IH, Kim N, Kim S, Toda K, Catavero CM, Courtland JL, Yin HH, and Soderling SH (2020). Dysregulation of the synaptic cytoskeleton in the PFC drives neural circuit pathology, leading to social dysfunction. Cell Rep. 32, 107965. 10.1016/j.celrep.2020.107965. [PubMed: 32726629]

Landis D, Courtney W, Dieringer C, Kelly R, King M, Miller B, Wang R, Wood D, Turner JA, and Calhoun VD (2016). COINS Data Exchange: an open platform for compiling, curating, and disseminating neuroimaging data. Neuroimage 124, 1084–1088. [PubMed: 26019122]

Leblond CS, Nava C, Polge A, Gauthier J, Huguet G, Lumbroso S, Giuliano F, Stordeur C, Depienne C, Mouzat K, et al. (2014). Meta-analysis of SHANK mutations in autism spectrum disorders: a gradient of severity in cognitive impairments. PLoS Genet. 10, e1004580. 10.1371/journal.pgen.1004580. [PubMed: 25188300]

Lee J, Chung C, Ha S, Lee D, Kim DY, Kim H, and Kim E (2015). Shank3-mutant mice lacking exon 9 show altered excitation/inhibition balance, enhanced rearing, and spatial memory deficit. Front. Cell. Neurosci 9, 94. 10.3389/fncel.2015.00094. [PubMed: 25852484]

Lee E, Rhim I, Lee JW, Ghim J-W, Lee S, Kim E, and Jung MW (2016). Enhanced neuronal activity in the medial prefrontal cortex during social approach behavior. J. Neurosci 36, 6926–6936. 10.1523/jneurosci.0307-16.2016. [PubMed: 27358451]

Levet F, Tønnesen J, Nägerl UV, and Sibarita J-B (2020). SpineJ: a software tool for quantitative analysis of nanoscale spine morphology. Methods 174, 49–55. 10.1016/j.ymeth.2020.01.020. [PubMed: 32006677]

Li Y, Zhu Y, Nguchu BA, Wang Y, Wang H, Qiu B, and Wang X (2020). Dynamic functional connectivity reveals abnormal variability and hyper-connected pattern in autism spectrum disorder. Autism Res. 13, 230–243. 10.1002/aur.2212. [PubMed: 31614075]

Liang B, Zhang L, Barbera G, Fang W, Zhang J, Chen X, Chen R, Li Y, and Lin D-T (2018). Distinct and dynamic ON and OFF neural ensembles in the prefrontal cortex code social exploration. Neuron 100, 700–714.e9. 10.1016/j.neuron.2018.08.043. [PubMed: 30269987]

Lynch CJ, Uddin LQ, Supekar K, Khouzam A, Phillips J, and Menon V (2013). Default mode network in childhood autism: posteromedial cortex heterogeneity and relationship with social deficits. Biol. Psychiatry 74, 212–219. 10.1016/j.biopsych.2012.12.013. [PubMed: 23375976]

Matas E, Maisterrena A, Thabault M, Balado E, Francheteau M, Balbous A, Galvan L, and Jaber M (2021). Major motor and gait deficits with sexual dimorphism in a Shank3 mutant mouse model. Mol. Autism 12, 2. 10.1186/s13229-020-00412-8. [PubMed: 33468258]

Mattis J, Tye KM, Ferenczi EA, Ramakrishnan C, O'Shea DJ, Prakash R, Gunaydin LA, Hyun M, Fenno LE, Gradinaru V, et al. (2012). Principles for applying optogenetic tools derived from direct comparative analysis of microbial opsins. Nat. Methods 9, 159–172. 10.1038/nmeth.1808.

Moessner R, Marshall CR, Sutcliffe JS, Skaug J, Pinto D, Vincent J, Zwaigenbaum L, Fernandez B, Roberts W, Szatmari P, and Scherer SW (2007). Contribution of SHANK3 mutations to autism spectrum disorder. Am. J. Hum. Genet 81, 1289–1297. 10.1086/522590. [PubMed: 17999366]

Monteiro P, and Feng G (2017). SHANK proteins: roles at the synapse and in autism spectrum disorder. Nat. Rev. Neurosci 18, 147–157. 10.1038/nrn.2016.183. [PubMed: 28179641]

Murugan M, Jang HJ, Park M, Miller EM, Cox J, Taliaferro JP, Parker NF, Bhave V, Hur H, Liang Y, et al. (2017). Combined social and spatial coding in a descending projection from the prefrontal cortex. Cell 171, 1663–1677.e16. 10.1016/j.cell.2017.11.002. [PubMed: 29224779]

Nelson SB, and Valakh V (2015). Excitatory/inhibitory balance and circuit homeostasis in autism spectrum disorders. Neuron 87, 684–698. 10.1016/j.neuron.2015.07.033. [PubMed: 26291155]

Pagani M, Bertero A, Liska A, Galbusera A, Sabbioni M, Barsotti N, Colenbier N, Marinazzo D, Scattoni ML, Pasqualetti M, and Gozzi A (2019). Deletion of autism risk gene Shank3 disrupts prefrontal connectivity. J. Neurosci. 39, 5299–5310. 10.1523/jneurosci.2529-18.2019. [PubMed: 31061091]

Park Y-G, Sohn CH, Chen R, Mccue M, Yun DH, Drummond GT, Ku T, Evans NB, Oak HC, Trieu W, et al. (2019). Protection of tissue physicochemical properties using polyfunctional crosslinkers. Nat. Biotechnol 37, 73–83. 10.1038/nbt.4281.

Peça J, Feliciano C, Ting JT, Wang W, Wells MF, Venkatraman TN, Lascola CD, Fu Z, and Feng G (2011). Shank3 mutant mice display autistic-like behaviours and striatal dysfunction. Nature 472, 437–442. 10.1038/nature09965. [PubMed: 21423165]

Pnevmatikakis EA, Soudry D, Gao Y, Machado TA, Merel J, Pfau D, Reardon T, Mu Y, Lacefield C, Yang W, et al. (2016). Simultaneous denoising, deconvolution, and demixing of calcium imaging data. Neuron 89, 285–299. 10.1016/j.neuron.2015.11.037. [PubMed: 26774160]

Power JD, Barnes KA, Snyder AZ, Schlaggar BL, and Petersen SE (2012). Spurious but systematic correlations in functional connectivity MRI networks arise from subject motion. Neuroimage 59, 2142–2154. [PubMed: 22019881]

Power JD, Mitra A, Laumann TO, Snyder AZ, Schlaggar BL, and Petersen SE (2014). Methods to detect, characterize, and remove motion artifact in resting state fMRI. Neuroimage 84, 320–341. [PubMed: 23994314]

Pruim RHR, Mennes M, van Rooij D, Llera A, Buitelaar JK, and Beckmann CF (2015). ICA-AROMA: a robust ICA-based strategy for removing motion artifacts from fMRI data. Neuroimage 112, 267–277. [PubMed: 25770991]

Riddle K, Cascio CJ, and Woodward ND (2017). Brain structure in autism: a voxel-based morphometry analysis of the autism brain imaging database exchange (ABIDE). Brain Imaging Behav. 11, 541–551. [PubMed: 26941174]

Rolls ET, Joliot M, and Tzourio-Mazoyer N (2015). Implementation of a new parcellation of the orbitofrontal cortex in the automated anatomical labeling atlas. Neuroimage 122, 1–5. [PubMed: 26241684]

Shirer WR, Ryali S, Rykhlevskaia E, Menon V, and Greicius MD (2012). Decoding subject-driven cognitive states with whole-brain connectivity patterns. Cereb. Cortex 22, 158–165. [PubMed: 21616982]

Sliwa J, and Freiwald WA (2017). A dedicated network for social interaction processing in the primate brain. Science 356, 745–749. 10.1126/science.aam6383. [PubMed: 28522533]

Smith SM, Fox PT, Miller KL, Glahn DC, Fox PM, Mackay CE, Filippini N, Watkins KE, Toro R, Laird AR, and Beckmann CF (2009). Correspondence of the brain's functional architecture during activation and rest. Proc. Natl. Acad. Sci. U S A 106, 13040–13045. 10.1073/pnas.0905267106. [PubMed: 19620724]

Supekar K, Uddin LQ, Khouzam A, Phillips J, Gaillard WD, Kenworthy LE, Yerys BE, Vaidya CJ, and Menon V (2013). Brain hyperconnectivity in children with autism and its links to social deficits. Cell Rep. 5, 738–747. 10.1016/j.celrep.2013.10.001. [PubMed: 24210821]

Tervo DG, Hwang BY, Viswanathan S, Gaj T, Lavzin M, Ritola KD, Lindo S, Michael S, Kuleshova E, Ojala D, et al. (2016). A designer AAV variant permits efficient retrograde Access to projection neurons. Neuron 92, 372–382. 10.1016/j.neuron.2016.09.021. [PubMed: 27720486]

Ting JT, Daigle TL, Chen Q, and Feng G (2014). Acute brain slice methods for adult and aging animals: application of targeted patch clamp analysis and optogenetics. In Patch-clamp Methods and Protocols (Springer).

Treder MS (2020). MVPA-light: a classification and regression toolbox for multi-dimensional data. Front. Neurosci 14, 289. [PubMed: 32581662]

Tsien JZ, Chen DF, Gerber D, Tom C, Mercer EH, Anderson DJ, Mayford M, Kandel ER, and Tonegawa S (1996). Subregion-and cell type–restricted gene knockout in mouse brain. Cell 87, 1317–1326. 10.1016/s0092-8674(00)81826-7. [PubMed: 8980237]

Uddin LQ, Supekar K, and Menon V (2013). Reconceptualizing functional brain connectivity in autism from a developmental perspective. Front. Hum. Neurosci 7, 458. [PubMed: 23966925]

von Neumann J, Kent RH, Bellinson HR, and Hart BI (1941). The mean square successive difference. Ann. Math. Stat 12, 153–162. 10.1214/aoms/1177731746.

Wang X, Mccoy PA, Rodriguiz RM, Pan Y, Je HS, Roberts AC, Kim CJ, Berrios J, Colvin JS, Bousquet-Moore D, et al. (2011). Synaptic dysfunction and abnormal behaviors in mice lacking major isoforms of Shank3. Hum. Mol. Genet 20, 3093–3108. 10.1093/hmg/ddr212. [PubMed: 21558424]

Wang P, Chen T, Sakurai K, Han B-X, He Z, Feng G, and Wang F (2012). Intersectional Cre driver lines generated using split-intein mediated split-Cre reconstitution. Sci. Rep 2, 497. 10.1038/srep00497. [PubMed: 22773946]

Wang X, Bey AL, Katz BM, Badea A, Kim N, David LK, Duffney LJ, Kumar S, Mague SD, Hulbert SW, et al. (2016). Altered mGluR5-Homer scaffolds and corticostriatal connectivity in a Shank3 complete knockout model of autism. Nat. Commun 7, 11459. 10.1038/ncomms11459. [PubMed: 27161151]

Werling DM, and Geschwind DH (2013). Sex differences in autism spectrum disorders. Curr. Opin. Neurol 26, 146–153. 10.1097/wco.0b013e32835ee548. [PubMed: 23406909]

Yi F, Danko T, Botelho SC, Patzke C, Pak C, Wernig M, and Südhof TC (2016). Autism-associated SHANK3 haploinsufficiency causes Ih channelopathy in human neurons. Science 352, aaf2669. 10.1126/science.aaf2669. [PubMed: 26966193]

Yizhar O, Fenno LE, Prigge M, Schneider F, Davidson TJ, O'Shea DJ, Sohal VS, Goshen I, Finkelstein J, Paz JT, et al. (2011). Neocortical excitation/inhibition balance in information processing and social dysfunction. Nature 477, 171–178. 10.1038/nature10360. [PubMed: 21796121]

Yoo T, Cho H, Park H, Lee J, and Kim E (2019). Shank3 exons 14–16 deletion in glutamatergic neurons leads to social and repetitive behavioral deficits associated with increased cortical layer 2/3 neuronal excitability. Front. Cell. Neurosci 13, 458. 10.3389/fncel.2019.00458. [PubMed: 31649512]

Zhang Y, Brady M, and Smith S (2001). Segmentation of brain MR images through a hidden Markov random field model and the expectation-maximization algorithm. IEEE Trans. Med. Imaging 20, 45–57. 10.1109/42.906424. [PubMed: 11293691]

Zhou Y, Sharma J, KE Q, Landman R, Yuan J, Chen H, Hayden DS, Fisher JW, Jiang M, Menegas W, et al. (2019). Atypical behaviour and connectivity in SHANK3-mutant macaques. Nature 570, 326–331. 10.1038/s41586-019-1278-0. [PubMed: 31189958]

Zingg B, Chou X-L, Zhang Z-G, Mesik L, Liang F, Tao HW, and Zhang LI (2017). AAV-mediated anterograde transsynaptic tagging: mapping corticocollicular input-defined neural pathways for defense behaviors. Neuron 93, 33–47. 10.1016/j.neuron.2016.11.045. [PubMed: 27989459]

Highlights

- Circuit-selective mutation (ctMUT) of *Shank3* in the PFC-BLA circuit

- *Shank3* ctMUT alters neuronal morphology, circuit activity, and reduces sociability

- Human ASD patients show similar abnormal mPFC-amygdala functional connectivity

- *Shank3* ctMUT disrupts temporal correlation of neural activity with social behavior
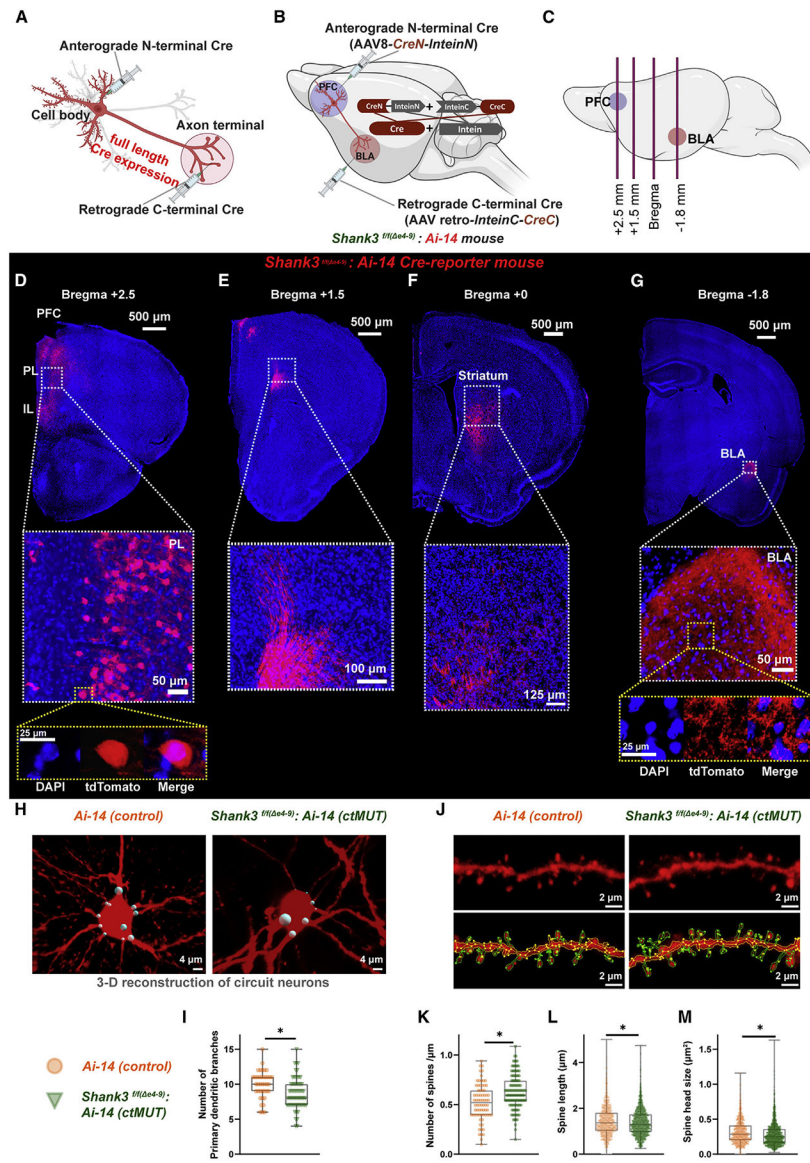
Figure 1. Shank3 mutation alters neuronal morphology in the PFC-BLA circuit

(A) Schematic illustration of circuit-selective Cre expression in a circuit neuron.

(B) Schematic of *in vivo* circuit-selective *Shank3* mutation in the PFC neurons projecting to the BLA.

(C) Coordinates of coronal slices for representative images in (D)–(G).

(D) Representative section showing tdTomato-expressing cell bodies in PL and IL areas of the PFC.

(E–G) Axonal fibers pass through the medial part of the striatum (E and F) and terminate in the BLA (G).

(H–M) Morphological analyses of neuronal structures from clarified brains.

(H) Representative PFC-BLA circuit neurons in *Ai-14* (control) and *Shank3 f/f*:*Ai-14* (ctMUT) mice.

(I) Mean number of primary dendrites in control PFC-BLA circuit neurons (n = 39 neurons from 4 mice) and ctMUT neurons (n = 62, from 6 mice) (p < 0.01).

(J) Representative dendrite images of control and ctMUT groups.

(K–M) Quantification of spine density (K; p < 0.0001), spine length (L; p < 0.05), and spine-head size (M; p < 0.0001) (control: n = 779 spines; ctMUT: n = 1,548 spines). *p < 0.05. Box and whisker plots display the median, upper and lower quartiles, and minimum and maximum values.
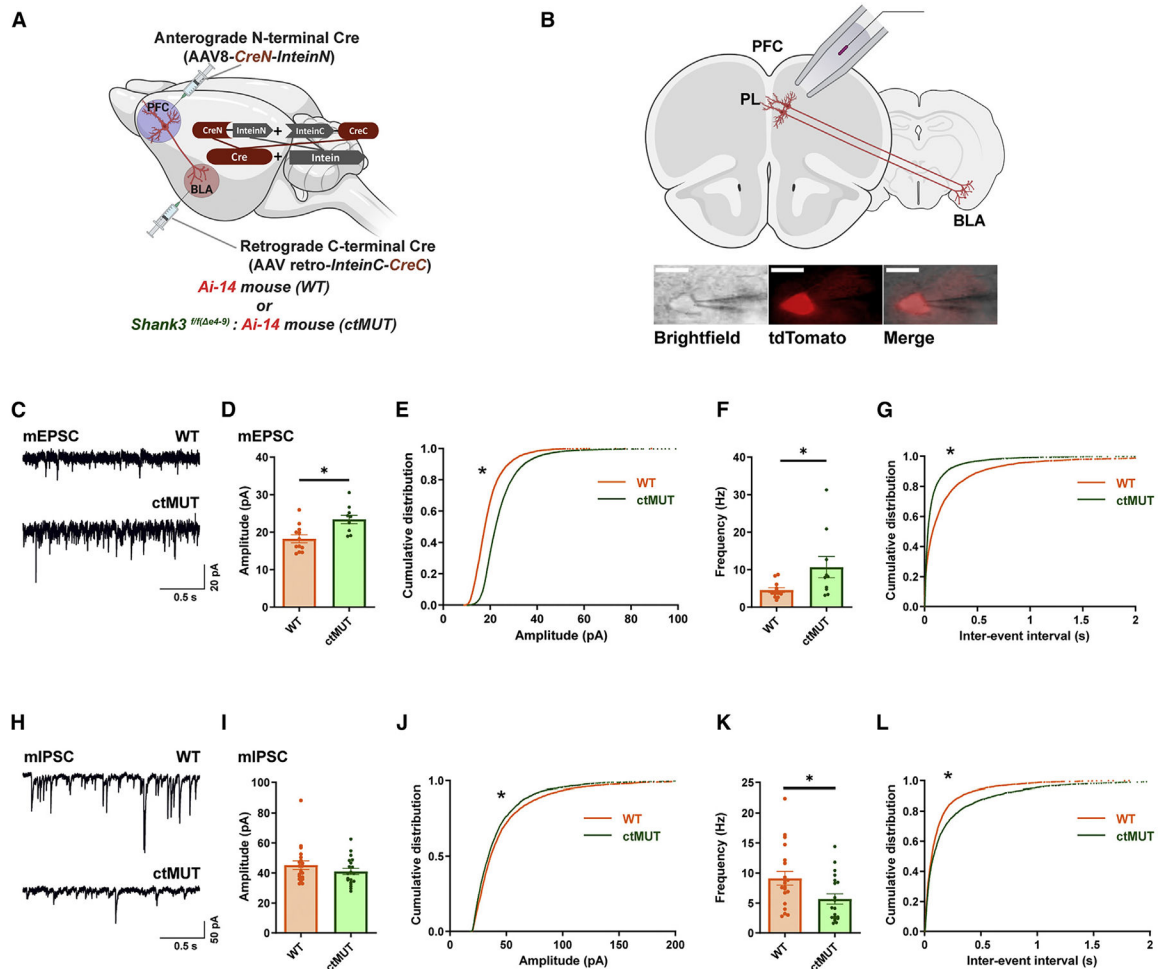
Figure 2. Shank3 ctMUT alters post-synaptic transmission in the PFC-BLA circuit neurons

(A) Schematic representation of split-Cre reconstitution in the PFC-BLA circuit of WT (Ai-14 Cre-reporter) mice and ctMUT (Shank3$^{f/f}$: Ai-14) mice.

(B) Schematic representation of whole-cell patch-clamp recording from PFC-BLA circuit neurons. Bottom panels show a representative patch-clamp recording on tdTomato-positive circuit neuron. Scale bar: 20 μm.

(C–G) mEPSC of neurons in WT (n = 12 from 3 mice) and ctMUT mice (n = 10 from 3 mice).

(C) Representative mEPSC traces of WT circuit neurons and ctMUT neurons in the PL.

(D) Mean amplitude of mEPSC (p < 0.01).

(E) Cumulative probability of mEPSC amplitudes (Kolmogorov-Smirnov [KS] test, p < 0.0001).

(F) Mean frequency of mEPSC (p < 0.05).

(G) Cumulative probability of inter-event intervals of mEPSC (KS test, p < 0.0001).

(H–L) mIPSC of neurons in WT (n = 20 from 6 mice) and ctMUT mice (n = 20 from 4 mice).

(H) Representative mIPSC traces of WT circuit neurons and ctMUT neurons in the PL.

(I) Mean amplitude of mIPSC (p > 0.24).

(J) Cumulative probability of mIPSC amplitudes (KS test, $p < 0.0001$).

(K) Mean frequency of mIPSC ($p < 0.05$).

(L) Cumulative probability of inter-event intervals of mIPSC (KS test, $p < 0.0001$). $*p < 0.05$. Data are represented as mean ± SEM.

Figure 3. Shank3 PFC-BLA ctMUT disrupts sociability and induces neural hyper-activity

(A) Schematic of circuit-selective Cre and GCaMP7f expression within PFC-BLA circuit. Inset shows a representative image of real-time Ca^{2+} signals. Scale bar: 100 μm.

(B) Schematic representation of the round social arena (RSA). Three social behaviors were analyzed: S-Zone entry, sniffing, and reciprocal sniffing.

(C) Two-stage experimental protocol (empty and social). Representative heatmaps showing movement traces of WT and *Shank3* ctMUT mice.

(D–I) Social behaviors of WT (n = 8) and ctMUT (n = 10) mice.

(D and E) Total sniffing (D) and mean duration of sniffing (E) on social stimulus (p < 0.0001).

(F and G) Total duration in S-Zone (F; p < 0.001), and mean duration of S-Zone entry (G; p < 0.05).

(H and I) Total reciprocal sniffing (H; p < 0.01), and mean duration per bout (I; p = 0.86).

(J) Representative Ca^{2+} traces of both groups.

(K and L) Ca^{2+} transient amplitude (K) and amplitude variance (L) in empty and social stages (p < 0.0001; WT: n = 675 from 8 mice; ctMUT: n = 1,112 from 10 mice).

(M) Correlations of Ca^{2+} transient amplitude and amplitude variance in both groups (WT: r = 0.78, p < 0.0001; ctMUT: r = 0.79, p < 0.0001). Colored lines indicate exponential models fit to the data for each group. *p < 0.05.

Bar graphs (D–I) are presented as mean ± SEM. Box and whisker plots (K and L) display the median, upper and lower quartiles, and minimum and maximum values.
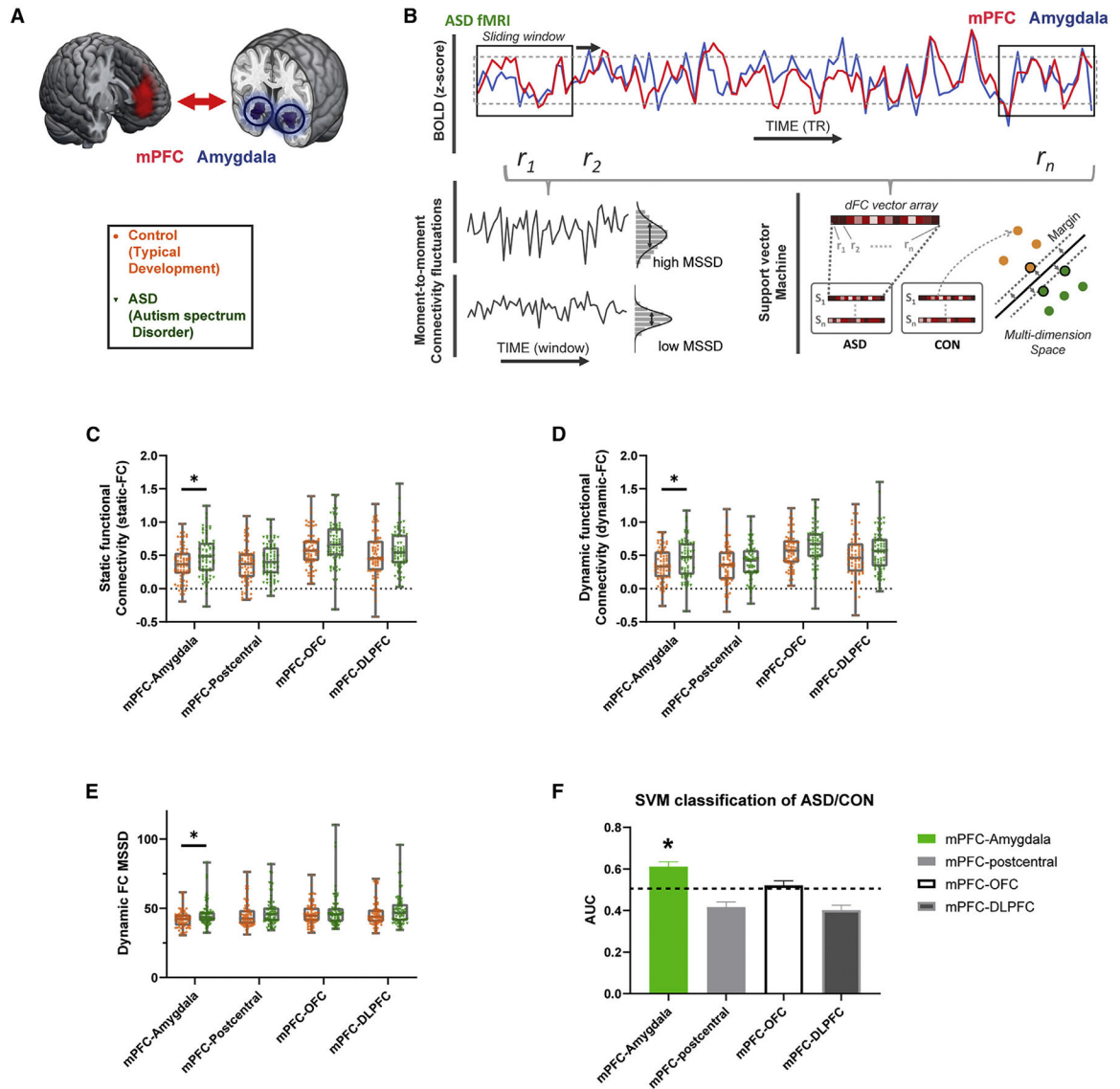
Figure 4. Human ASD patients show PFC-BLA hyper-connectivity and -variability of connectivity

(A) Regions of interest (ROIs) for functional connectivity analyses: the medial prefrontal cortex (mPFC: red), and the amygdala (blue).

(B) Representative static functional connectivity (static-FC), the dynamic functional connectivity (dynamic-FC), the mean square successive difference (MSSD), and the support vector machine (SVM) classification. The static-FC used the entire time-series (dotted square), and the dynamic-FC used a moving sliding window (solid square). The dynamic-FC series were also used for MSSD and SVM classification.

(C–F) Human neuroimaging results (Control: n = 72; ASD: n = 72).

(C) Static-FC ($p < 0.05$).

(D) Dynamic-FC ($p < 0.05$).

(E) Statistical analysis of MSSD showing a hyper-variant mPFC-amygdala connection in ASD ($p < 0.05$).

(F) Result of the SVM classification using dynamic-FC values. mPFC-amygdala pair showed a significantly higher classification accuracy against chance level (50%; dashed line) over accuracy distribution obtained from 5,000 label-shuffled permutations (p < 0.05). *p < 0.05.

Bar graphs (F) are presented as mean ± SEM. Box and whisker plots (C–E) display the median, upper and lower quartiles, and minimum and maximum values.
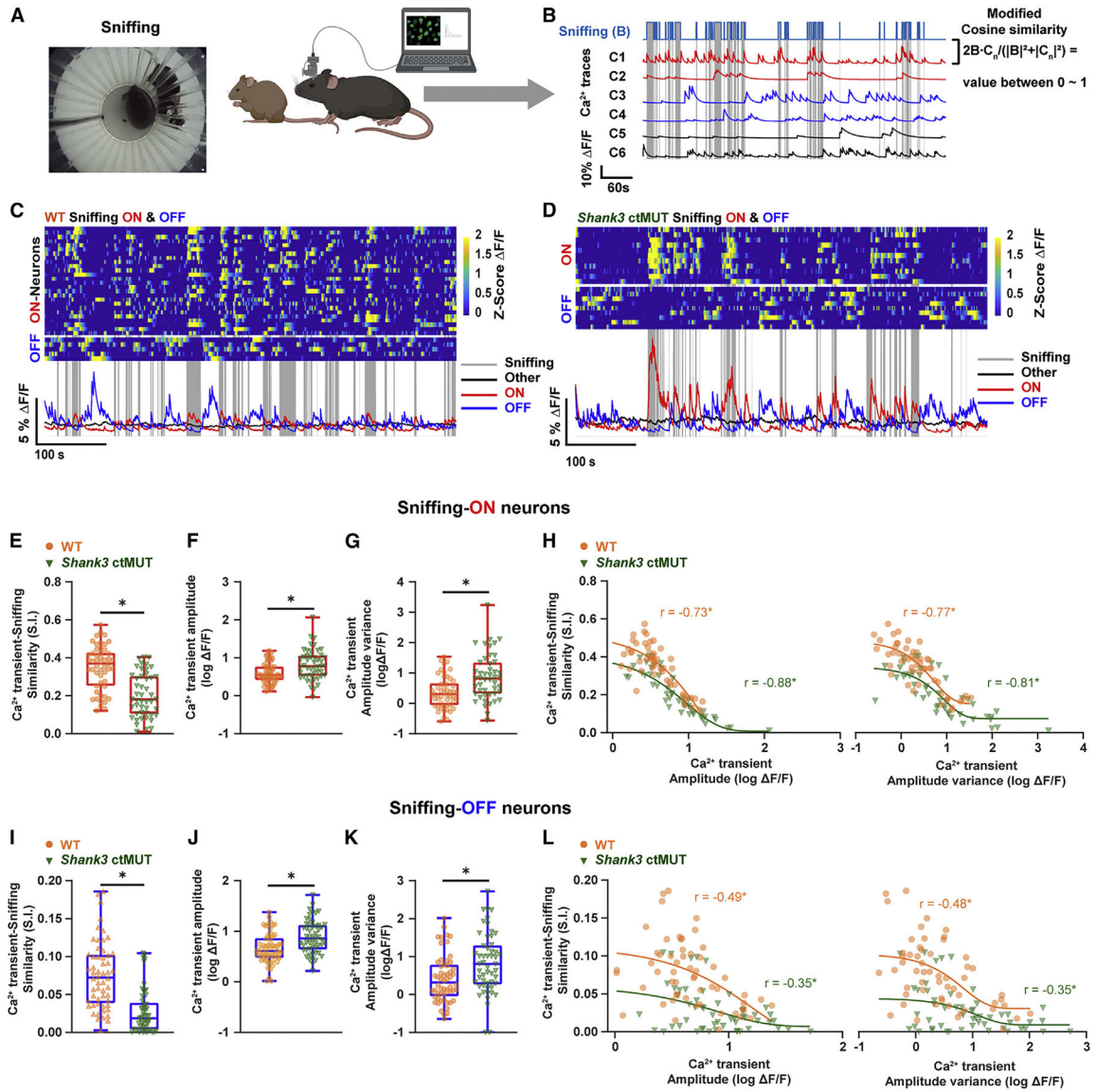
Figure 5. Shank3 ctMUT reduces the temporal correlation of the PFC-BLA circuit activity with sniffing behavior

(A) Schematic illustration for simultaneous observation of sniffing behavior and Ca^{2+} activity.

(B) Calculation of similarity between a sniffing-behavior vector (gray vertical lines) and a Ca^{2+} trace of circuit neurons using modified cosine similarity.

(C) Example ON (n = 26) and OFF (n = 5) neurons for sniffing behavior recorded in a WT mouse. Heatmaps in the top panel show normalized Ca^{2+} traces of individual neurons, and the bottom panel shows averaged Ca^{2+} traces of ON, OFF, and Other neurons. The gray lines indicate sniffing-behavior epochs.

(D) Example ON (n = 11) and OFF (n = 9) neurons for sniffing behavior recorded in a ctMUT mouse.

(E–H) Sniffing-ON neurons (WT: n = 51 from 8 mice; ctMUT: n = 47 from 10 mice).

(E) Similarity between sniffing-ON Ca^{2+} trace and sniffing (p < 0.0001).

(F) Sniffing-ON Ca^{2+} transient amplitude ($p < 0.005$).

(G) Sniffing-ON Ca^{2+} transient amplitude variance ($p < 0.001$).

(H) (Left) Negative correlation between sniffing-ON Ca^{2+} transient amplitude and the Ca^{2+} trace-sniffing similarity (WT: $r = -0.73$, $p < 0.0001$; ctMUT: $r = -0.88$, $p < 0.0001$). (Right) Negative correlation between sniffing-ON Ca^{2+} transient amplitude variance and Ca^{2+} trace-sniffing similarity (WT: $r = -0.77$, $p < 0.0001$; ctMUT: $r = -0.81$, $p < 0.0001$).

(I–L) Sniffing-OFF neurons (WT: n = 56 from 8 mice; ctMUT: n = 53 from 10 mice).

(I) Similarity between sniffing-OFF Ca^{2+} trace and sniffing ($p < 0.0001$).

(J) Sniffing-OFF Ca^{2+} transient amplitude ($p < 0.001$).

(K) Sniffing-OFF Ca^{2+} transient amplitude variance ($p < 0.005$).

(L) (Left) Negative correlation between sniffing-OFF Ca^{2+} transient amplitude and Ca^{2+}trace-sniffing similarity (WT: $r = -0.49$, $p < 0.001$; ctMUT: $r = -0.35$, $p < 0.01$). (Right) Negative correlation between sniffing-OFF Ca^{2+} transient amplitude variance and Ca^{2+} trace-sniffing similarity (WT: $r = -0.48$, $p < 0.0005$; ctMUT: $r = -0.35$, $p < 0.01$). *$p < 0.05$.

Box and whisker plots (E–G and I–K) display the median, upper and lower quartiles, and minimum and maximum values. Colored lines in (H) and (L) indicate exponential models fit to the data for each group.
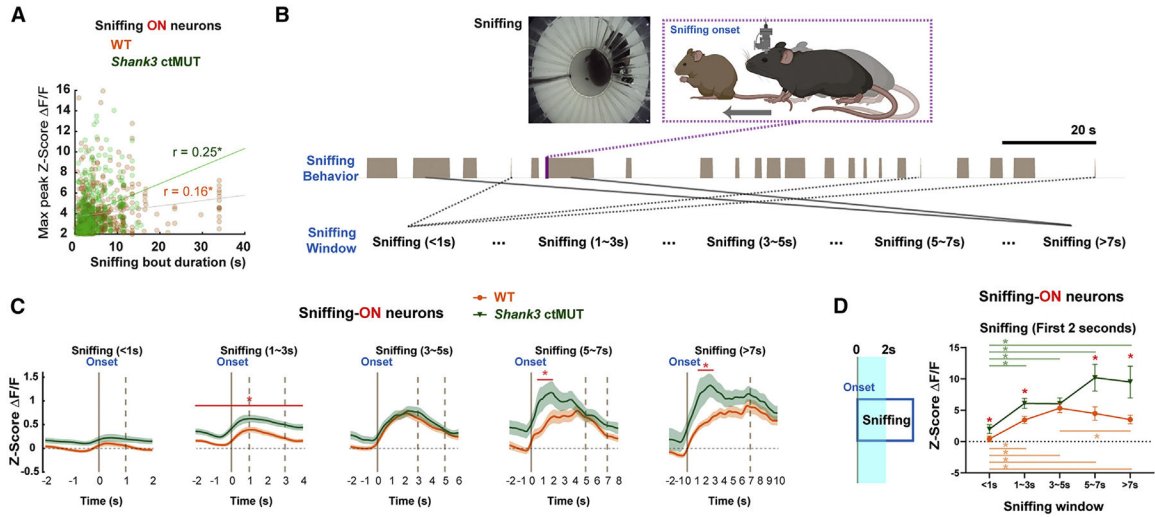
Figure 6. Shank3 ctMUT enhances neural activity proportional to the duration of social behavior

(A, C, and D) Sniffing-ON neurons (WT: n = 532; ctMUT: n = 366 neuron-sniffing-duration pairs).

(A) Correlation between sniffing-bout duration and maximum peak normalized Ca^{2+} transient amplitude of sniffing-ON neurons during sniffing (WT: r = 0.16, p < 0.0001; ctMUT: r = 0.25, p < 0.0001).

(B) A schematic illustration for separating Ca^{2+} transient data into various time windows according to the duration of behavioral epochs.

(C) Normalized Ca^{2+} transient of sniffing-ON neurons, aligned to the onsets of sniffing in multiple time windows (*p < 0.05).

(D) Schematic illustration of analysis during sniffing (cyan; 2 s after sniffing onset). Analysis of all behavioral windows (sniffing duration) between groups (*p < 0.05). *p < 0.05. Data represent mean ± SEM.
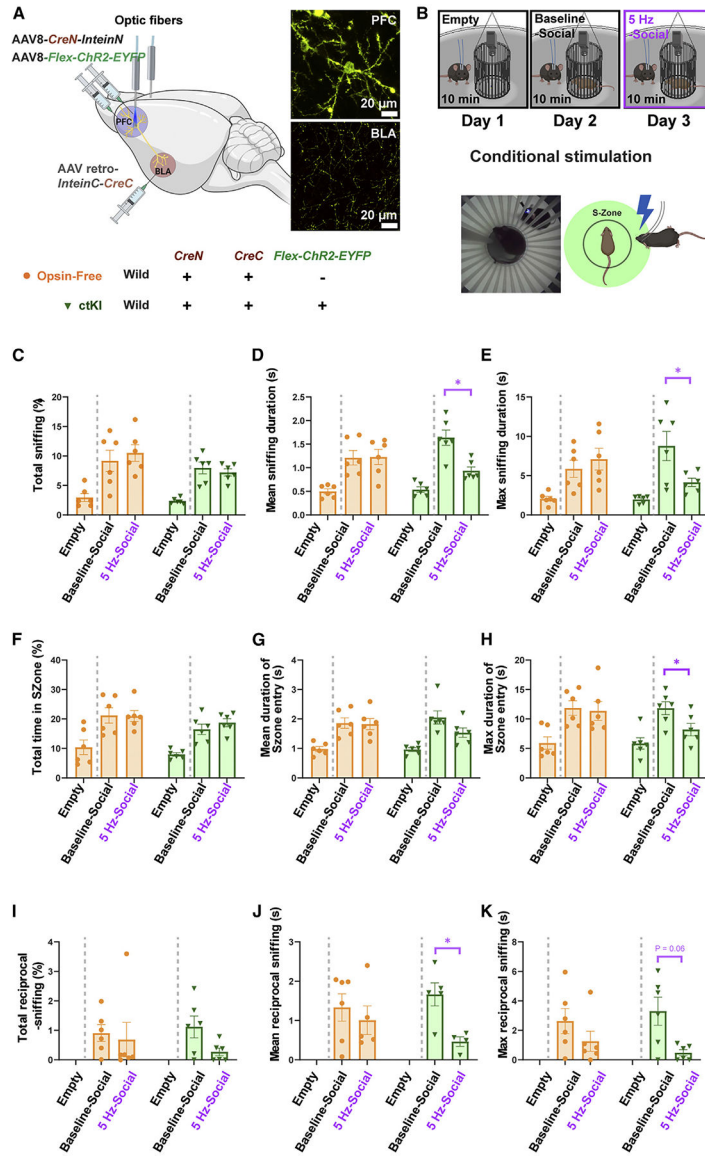
Figure 7. Conditional PFC-BLA circuit activation disrupts social behaviors

(A) A schematic illustration of viral-injection strategy and optic-fiber implantation. Right panel shows ChR2-EYFP expressions in the PFC (top; cell bodies) and in the BLA (bottom; axonal fibers).

(B) Experimental procedure consisting of three 10 min tests (empty, baseline-social, 5 Hz-social). Conditional optical stimulation was given upon the test mouse's entry into the S-Zone.

(C–K) Social behaviors of mice (WT: n = 6; ctMUT: n = 6).

(C–E) Analysis for sniffing.

(C) Total sniffing.

(D) Mean duration of sniffing per bout (p < 0.01).

(E) Maximum duration of sniffing per bout (p < 0.05).

(F–H) Analysis for S-zone.

(F) Total duration in S-Zone.

(G) Mean duration of S-Zone entry per visit (p = 0.069).

(H) Maximum duration of S-Zone entry per visit (p < 0.05).

(I–K) Analysis for reciprocal sniffing.

(I) Total reciprocal sniffing.

(J) Mean duration of reciprocal sniffing per bout (p < 0.05).

(K) Maximum duration of reciprocal sniffing per bout (p = 0.06). *p < 0.05. Significant differences from the empty stage to baseline-social stage are not presented here. Data are presented as mean ± SEM.

KEY RESOURCES TABLE

REAGENT or RESOURCE	SOURCE	IDENTIFIER
Bacterial and virus strains		
AAV2/8-*Ef1a-Flex-GFP*	Kim et al. (2013) https://doi.org/10.1523/JNEUROSCI.0035%5f13.2013	N/A
AAV2/8-*Ef1a-CreN-InteinN*	This Paper	N/A
AAV2/9-*Ef1a-CreN-InteinN*	This Paper	N/A
Retrograde AAV-*Ef1a-InteinC-CreC*	This Paper	N/A
Retrograde AAV-*Ef1a-CreN-InteinN*	This Paper	N/A
AAV2/9-*hSyn-Cre*	This Paper	N/A
AAV2/8-*Ef1a-Flex-hChR2(H134R)-EYFP-WPRE-HGHpA*	Purification using Addgene # 20298 plasmid Deposited by Karl Deisseroth (RRID: Addgene_20298)	N/A
pGP-AAV2/9-*Syn-Flex-jGCaMP7f-WPRE*	Addgene Dana et al., 2019 https://doi.org/10.1038/s41592-019-0435-6. Epub 2019 Jun 17	Addgene viral prep# 104492-AAV9
AAV *DJ-Flex-EF1a-eArch3.0-EYFP*	Stanford vector core https://doi.org/10.1038/nmeth.1808	GVVC-AAV-55
AAV9-*hSyn-GFP*	This Paper	N/A
Escherichia coli; Stbl3	Thermo Fisher	C737303
Chemicals, peptides, and recombinant proteins		
DAPI	Sigma	10236276001
Isoflurane	Henry Schein	1182097
C&B Metabond® Quick Adhesive Cement System	Parkell	S380
Ethicon Suture 3/0	Ethicon	669H
Heparin sodium salt	Sigma	H3393
Triton X-100	IBI scientific	IB07100
Glycerol Proteomics Grade	VWR	VWRVM152-1L
Paraformaldehyde, PRILLS	Electron Microscopy Sciences	19202
Paraformaldehyde 32% solution, EM Grade	Electron Microscopy Sciences	15714-S
Tissue-Tek® O.C.T. Compound	Sakura	4583
Mounting medium: ProLong Glass	Invitrogen	P36980
PEI	Polyscience	24765
Benzonase	Novagen	70664
Phenol red	Sigma	P0290
Optiprep	Sigma	D1556
SHIELD Buffer solution	LifeCanvas Technologies	CAT #: SH-BS
SHIELD Epoxy solution	LifeCanvas Technologies	CAT #: SH-EX
SHIELD ON buffer	LifeCanvas Technologies	CAT #: SH-ON
SmartClear Clearing Buffer Type A & B	LifeCanvas Technologies	CAT #: SC-B2001
EasyIndex Optical Clearing Solution	LifeCanvas Technologies	CAT #: EI-Z1001
DMEM Nutrient mix F12	Gibco	11320082
Opti-MEM	Gibco	31985070
Trypsin 0.05% EDTA	Corning	25300054

REAGENT or RESOURCE	SOURCE	IDENTIFIER
Penicillin Streptomycin Solution	Gibco	15140122
Heat Inactivated Fetal Bovine Serum	Gibco	10438026
Cholrea toxin subunit B-Alexa Fluor 488 conjugated	Invitrogen	C22841
Tetrodotoxin citrate	Tocris	1069/1
Picrotoxin	Sigma	P1675
D-AP5	Tocris	0106/10
DNQX	Sigma	D0540-50MG
Experimental models: Cell lines		
HEK293T	ATCC	CRL-11268
Experimental models: Organisms/strains		
Mouse: C57BL/6J	The Jackson Laboratory	#000664
Mouse: *Ai-14* (B6; 129S6-Gt (ROSA)26Sor^tm14(CAG-tdTomato)Hze/J)	The Jackson Laboratory	#007908
Mouse: *Shank3* $^{f/f(\ e4-9)}$	Yale University	N/A
Mouse: C3H/HeJ	The Jackson Laboratory	#000659
Recombinant DNA		
AAV-*Ef1a-Flex-GFP*	Kim et al. (2013) https://doi.org/10.1523/JNEUROSCI.0035-13.2013	N/A
AAV-*Ef1a-CreN-InteinN*	This Paper	N/A
AAV-*Ef1a-InteinC-CreC*	This Paper	N/A
AAV-*hSyn-Cre*	This Paper	N/A
AAV-*Ef1a-Flex-hChR2(H134R)-EYFP-WPRE-HGHpA*	Addgene Deposited by Karl Deisseroth (RRID: Addgene_20298)	Addgene plasmid # 20298
AAV2/8	Addgene Deposited by James M. Wilson (RRID: Addgene_112864)	Addgene plasmid # 112864
AAV2/9	Addgene Deposited by James M. Wilson (RRID: Addgene_112865)	Addgene plasmid # 112865
Retrograde AAV	Addgene Tervo et al. (2016) https://doi.org/10.1016/j.neuron.2016.09.021	Addgene plasmid # 81070
pAd-deltaF	Addgene Deposited by James M. Wilson (RRID: Addgene_112867)	Addgene plasmid # 112867
Software and algorithms		
Prism 9.0	GraphPad https://www.graphpad.com	N/A
SPSS 25	IBM	N/A
MATLAB R2020a	Mathworks https://www.ibm.com	N/A
Classification Learner ToolBox	Mathworks https://www.mathworks.com	N/A
Python 3.4	Python https://www.python.org/	N/A
Scikit-Learn package	Python https://scikit-learn.org/stable/	N/A

REAGENT or RESOURCE	SOURCE	IDENTIFIER
NetworkX package	Python https://networkx.org/	N/A
nVista Data Acquisition Software	Inscopix https://www.inscopix.com/	N/A
Inscopix Data Processing Software	Inscopix https://www.inscopix.com/	N/A
CNMFe	Pnevmatikakis et al. (2016) https://doi.org/10.1016/j.neuron.2015.11.037	N/A
EthoVisionXT	Noldus https://www.noldus.com/	N/A
Zen software	Zeiss https://www.zeiss.com/	N/A
SyGlass	Isto Visio RRID:SCR_017961	N/A
ImageJ	ImageJ https://imagej.nih.gov/ij/	N/A
SpineJ	Levet et al. (2020) https://doi.org/10.1016/j.ymeth.2020.01.020 https://github.com/flevet/SpineJ	N/A
Sketch	Arduino https://www.arduino.cc/	N/A
Inventor	Autodesk https://www.autodesk.com/	N/A
FMRIB software Library	Jenkinson et al. (2012) https://doi.org/10.1016/j.neuroimage.2011.09.015 https://www.fmrib.ox.ac.uk/datasets/techrep/tr04ss2/tr04ss2/node19.html	N/A
ICA-AROMA	Pruim et al. (2015) https://doi.org/10.1016/j.neuroimage.2015.02.064 https://github.com/maartenmennes/ICA-AROMA	N/A
MELODIC	FMRIB software Library Beckmann and Smith (2004) https://doi.org/10.1109/TMI.2003.822821	N/A
ANTs	Avants et al. (2011) https://doi.org/10.1016/j.neuroimage.2010.09.025 https://github.com/ANTsX/ANTs/	N/A
FAST	Zhang et al. (2001) FMRIB software Library https://doi.org/10.1109/42.906424	N/A
90 fROIs	Shirer et al. (2012) roi: https://doi.org/10.1093/cercor/bhr099 https://findlab.stanford.edu/functional_ROIs.html	N/A
AAL2 atlas	Rolls et al. (2015) https://doi.org/10.1016/j.neuroimage.2015.07.075 https://www.gin.cnrs.fr/en/	N/A
MVPA-Light	Treder (2020) https://doi.org/10.3389/fnins.2020.00289 https://github.com/treder/MVPA-Light	N/A
pCLAMP10	Molecular Devices	
BioRender	https://biorender.com/	N/A

REAGENT or RESOURCE	SOURCE	IDENTIFIER
ABIDE dataset	Mind Research Network Collaborative informatics and neuroimaging suite (COINS) data exchange Landis et al. (2016) https://doi.org/10.1016/j.neuroimage.2015.05.049 https://coins.trendscenter.org/	N/A
Lindquist Dynamic Correlation Toolbox	https://github.com/canlab/ Lindquist_Dynamic_Correlation/tree/master/ DCC_toolbox	N/A
Deposited data		
Round Social Arena	Zenodo: https://doi.org/10.5281/zenodo.6536336; https://zenodo.org/badge/latestdoi/333558926	N/A
Other		
nVista	Inscopix https://www.inscopix.com/	N/A
Dual Channel Optogenetics-LED	Prizmatix https://www.prizmatix.com	N/A
Fiber-Optic Rotary Joint	Doric	FRJ_1 × 1_FC
Splitter Branching Fiber-Optic Patch Cords	Doric	N/A
Rotamex	Columbus Instruments http://www.colinst.com/	N/A
Oculus Rift S	Oculus https://www.oculus.com/	N/A
Mini USB IO Box	Noldus https://www.noldus.com/ethovision-xt/io-box	N/A
Arduino UNO	Arduino https://www.arduino.cc/	N/A
Basler Ace color camera with Gigabit Ethernet Interface	Basler https://www.baslerweb.com/	N/A
SVPRO Fisheye Lens 180 Degree USB Camera Module HD 1080P, Sony IMX322 USB Camera Board with Microphone	SVPRO	N/A
CELENA-S Digital Imaging System	Logos biosystems https://logosbio.com/	N/A
Zeiss LSM 710 Confocal Microscope	Zeiss https://www.zeiss.com/	LSM 710
Leica CM 1950 Cryostat	Leica https://www.leica-microsystems.com/	CM 1950
Vibratome 1000 Plus Sectioning System	Vibratome	N/A
Model 962 Dual Ultra Precise Small Animal Stereotaxic	David Kopf Instruments https://kopfinstruments.com/	Model 962
Nanoject II nanoliter injector	Drummond Scientific Company https://www.drummondsci.com/	N/A
V-1 Tabletop Active Scavenging Anesthesia Machine	VetEquip http://www.vetequip.com/	N/A
Model P-97 Flaming/brown micropipette puller	Sutter Instrument https://www.sutter.com/	P-97
Sorvall Legend X1 Centrifuge	Thermo Fisher	N/A
Sorvall Lynx 6000 Centrifuge	Thermo Fisher	N/A
Beckman L8-70M Ultracentrifuge	Beckman Coulter	N/A
Legend Micro21R Centrifuge	Thermo Fisher	N/A
1300 Series A2 Biosafety Cabinet	Thermo Fisher	Model 1385

REAGENT or RESOURCE	SOURCE	IDENTIFIER
Thermo Scientific CO2 Incubator	Thermo Fisher	Model 370
Isotemp Incubator	Thermo Fisher	151030513
SmartClear Pro II	LifeCanvas Technologies https://lifecanvastech.com	N/A
Form2 SLA 3D Printer	Formlabs https://formlabs.com	Form2
Dremel Digilab 3D20 3D Printer	Dremel Digilab https://digilab.dremel.com/	3D20
iQ5 Multicolor Real-Time PCR Detection System	BIO-RAD https://www.bio-rad.com	N/A
Leica VT1200S vibratome	Leica https://www.leica-microsystems.com/	VT1200S
CV-7B headstage	Molecular Devices	CV-7B
Multiclamp 700B	Molecular Devices	Multiclamp 700B
Digidata 1440A	Molecular Devices	Digidata 1440A
MPC-200	Sutter Instrument https://www.sutter.com/	MPC-200
ROE-200	Sutter Instrument https://www.sutter.com/	ROE-200
Olympus BX50WI Microscope		Olympus BX50WI
Advanced micro osmometer	Advanced Instruments. Inc.	Model 3300
Borosilicate Glass with Filament (O.D.: 1.2mm, I.D.: 0.94mm, 8cm length) for viral injection	Sutter Instrument https://www.sutter.com/	ITEM #: BF120-94-8
Borosilicate Glass Capillaries (O.D.: 1.5mm, I.D.: 1.12mm, 10cm length) for patch clamp	World precision instruments https://www.wpiinc.com/	TW150-4
Square Box Filament	Sutter Instrument https://www.sutter.com/	ITEM #: FB255B
ProView™ Lens Probe 1.0 diametter, ~4mm length	Inscopix https://www.inscopix.com/	1050-004605–IPN:100–001851
Formlabs Clear Resion V4	Formlabs https://formlabs.com	RS-F2-GPCL-04
White PLA Filament	Dremel Digilab https://digilab.dremel.com/	N/A
Fiber-optic probes (400mm fiber core diameter, 1.25mm OD ferrule, 0.5NA)	RWD Life Sciences Inc. https://www.rwdstco.com/	ITEM #: 807-00048-00
Amicon Ultra-15 Centrifugal Filters (100k MWCO)	Millipore Sigma	CAT #: UFC900308